Analysis, Control, and Design Optimization of Engineering Mechanics Systems

Esubalewe Lakie Yedeg

PhD Thesis, May 2016

Department of Computing Science
Umeå University
SE-901 87 Umeå
Sweden

Department of Computing Science
Umeå University
SE-901 87 Umeå, Sweden

yedegl@cs.umu.se

UMINF: 16.13
ISSN: 0348-0542
ISBN: 978-91-7601-497-4

Electronic version available at http://umu.diva-portal.org/
Printed by Print & Media, Umeå University
Umeå, Sweden 2016

Abstract

This thesis considers applications of gradient-based optimization algorithms to the design and control of some mechanics systems. The material distribution approach to topology optimization is applied to design two different acoustic devices, a reactive muffler and an acoustic horn, and optimization is used to control a ball pitching robot.

Reactive mufflers are widely used to attenuate the exhaust noise of internal combustion engines by reflecting the acoustic energy back to the source. A material distribution optimization method is developed to design the layout of sound-hard material inside the expansion chamber of a reactive muffler. The objective is to minimize the acoustic energy at the muffler outlet. The presence or absence of material is represented by design variables that are mapped to varying coefficients in the governing equation. An anisotropic design filter is used to control the minimum thickness of materials separately in different directions. Numerical results demonstrate that the approach can produce mufflers with high transmission loss for a broad range of frequencies.

For acoustic devices, it is possible to improve their performance, without adding extended volumes of materials, by an appropriate placement of thin structures with suitable material properties. We apply layout optimization of thin sound-hard material in the interior of an acoustic horn to improve its far-field directivity properties. Absence or presence of thin sound-hard material is modeled by a surface transmission impedance, and the optimization determines the distribution of materials along a "ground structure" in the form of a grid inside the horn. Horns provided with the optimized scatterers show a much improved angular coverage, compared to the initial configuration.

The surface impedance is handled by a new finite element method developed for Helmholtz equation in the situation where an interface is embedded in the computational domain. A Nitsche-type method, different from the standard one, weakly enforces the impedance conditions for transmission through the interface. As opposed to a standard finite-element discretization of the problem, our method seamlessly handles both vanishing and non-vanishing interface conditions. We show the stability of the method for a quite general class of surface impedance functions, provided that possible surface waves are sufficiently resolved by the mesh.

The thesis also presents a method for optimal control of a two-link ball pitching robot with the aim of throwing a ball as far as possible. The pitching robot is connected to a motor via a non-linear torsional spring at the shoulder joint. Constraints on the motor torque, power, and angular velocity of the motor shaft are included in the model. The control problem is solved by an interior point method to determine the optimal motor torque profile and release position. Numerical experiments show the effectiveness of the method and the effect of the constraints on the performance.

Sammanfattning

Denna avhandling använder sig av gradientbaserade optimeringsalgoritmer för design och styrning av ett antal mekaniksystem. Topologioptimering med materialdistrubutionsmetoden används för att formge två olika akustiska anordningar, en reaktiv ljuddämpare och ett akustiskt horn. Dessutom används en optimeringsmetod för att styra en bollkastande robot.

Reaktiva ljuddämpare används ofta för att dämpa avgasljudet hos förbränningsmotorer genom att reflektera den akustiska energin tillbaka till källan. En materialdistributionsmetod har utvecklats för att utforma fördelningen av ljudhårt material inuti expansionskammaren i en reaktiv ljuddämpare. Målet är att minimera den akustiska energin vid ljuddämparens utlopp. Närvaro eller frånvaro av material representeras av designvariabler som avbildas till varierande koefficienter i ljudutbredningsmodellens ekvation. Ett anisotropt designfilter används för att separat begränsa den minimala tillåtna materialtjockleken i olika riktningar. De numeriska resultaten visar att metoden kan generera ljuddämpare med höga transmissionsförluster för ett brett frekvensband.

För akustiska komponenter är det ofta möjligt att påverka prestanda, utan att behöva använda omfattande volymer av material, genom en lämplig placering av tunna strukturer med lämpliga materialegenskaper. Vi optimerar utbredningen av tunt ljudhårt material i det inre av ett akustiskt horn för att förbättra hornets spridningsegenskaper i fjärrfältet. Frånvaro eller närvaro av tunt ljudhårt material modelleras genom en varierande akustisk impedans över ett antal givna ytor, och en optimeringsalgoritm bestämmer fördelningen av material utmed en grundstruktur i form av ett galler inuti hornet. Hornen som är försedda med de optimerade spridarna visar en mycket förbättrad vinkeltäckning jämfört med den ursprungliga konfigurationen. Ytimpedanserna hanteras numeriskt med hjälp av en ny finita-elementmetod som utvecklats för Helmholtz ekvation i närvaro av impedansytor i beräkningsdomänen. En metod av Nitschetyp, som skiljer sig från standardversionen, används för en svag formulering av impedansenvillkoren. I motsats till standardmetoden för hantering av impedansytor klarar vår metod att sömlöst hantera fallen då transmissionsimpedansen är såväl noll som nollskild. Vi visar att metoden är stabil för en förhållandevis allmänn klass av ytimpedansfunktioner, förutsatt att eventuella ytvågor är tillräckligt upplösa av beräkningsnätet.

Avhandlingen presenterar också en metod för optimal styrning av en tvålänks bollkastande robot i syfte att kasta bollen en så lång sträcka som möjligt. Robotarmen är ansluten till en motor via en olinjär torsionsfjäder vid armens axelled. Begränsningar för motorns vridmoment samt kraften och vinkelhastigheten hos motoraxeln är inkluderade i modellen. Styrproblemet löses med hjälp av en inrepunktsmetod som bestämmer den optimala motormomentsprofilen samt frigöringsläget för bollen. Numeriska experiment påvisar metodens effektivitet och belyser de pålagda bivillkorens effekt på kastlängden.

Preface*

This thesis consists of introductions to the subject of topology optimization and Nitsche-type methods for interface problems and the following papers.

Paper I Esubalewe Lakie Yedeg, Eddie Wadbro, and Martin Berggren. Interior layout topology optimization of a reactive muffler. *Structural and Multidisciplinary Optimization*, vol. 53, pp. 645–656, 2016.

Paper II Esubalewe Lakie Yedeg, Eddie Wadbro, Peter Hansbo, Mats G. Larson, and Martin Berggren. A Nitsche-type Method for Helmholtz Equation with an Embedded Acoustically Permeable Interface. *Computer Methods in Applied Mechanics and Engineering*, vol. 304, pp. 479–500, 2016.

Paper III Esubalewe Lakie Yedeg, Eddie Wadbro, and Martin Berggren. Layout optimization of thin sound-hard material to improve the far-field directivity properties of an acoustic horn. Submitted for publication, 2016.

Paper IV Esubalewe Lakie Yedeg. On the use of thin structures to control the far-field properties of an acoustic device. *Technical Report UMINF 16.12*, Department of Computing Science, Umeå University, 2016.

Paper V Esubalewe Lakie Yedeg and Eddie Wadbro. State constrained optimal control of a ball pitching robot. *Mechanism and Machine Theory*, vol. 69, pp. 337–349, 2013.

This work has been financially supported in part by the Swedish Foundation for Strategic Research, Grant No. AM13-0029, and by the Swedish Research Council, Grant No. 621-2013-3706.

*The papers have been re-typeseted to fit the booklet's style. There may be minor typographical differences from the published papers.

Acknowledgement

This thesis would not have been possible without the inspiration, encouragement, and support of several individuals. I take this opportunity to give special thanks to the following people.

First and foremost, I would like to express my sincere gratitude to my scientific advisor, Martin Berggren for giving me the chance to join his research group and for his continuous guidance, inspiration, encouragement, and support. He has been a thoughtful and wonderful advisor, and without him this thesis would not have been completed or written. Martin, thank you for invaluable discussions and incredible feedback in my work. I have learned quite a lot from you.

I would also like to extend my appreciation to my co-advisor Eddie Wadbro for interesting and fruitful discussions. I am grateful for his boundless support, especially when I desire an advice on Matlab implementation. He was always open to me whenever I needed his advice on research or other issues.

My deep gratitude also goes to all colleagues at UMIT research lab and the Department of Computing Science for the friendly and pleasant working atmosphere. In particular, I am grateful to members of the Design and Optimization research group and system administrators.

I would like to extend my thanks to all Ethiopian friends who live in Umeå, especially Meseret, Anteneh, Ewnetu, and their families who made me feel at home during my stay here. Meseret you are special for my family and I really thank you for everything you have done. I am also thankful to Enideg and Fiseha for their support.

I would like to say a heartfelt thank you to my parents, Wubit Aragaw and Lakie Yedeg for always believing in me and for their unconditional support, encouragement, and prayers. Without their support and prayers this work would not have been possible. Wubit, I always love you, you played a major role in shaping my life and you have been the rock of our family. I am also grateful to my brother Bekalu Lakie, my uncle Ashagre Yedeg, and their families for supporting me in whatever way they could. I would also like to thank my parents-, brothers-, and sisters-in-law for their steady support and prayers.

Last but not least, my deep and special appreciation goes to my wife, Tigist Muluken, who has given me the strength, support, encouragement, and inspiration. Tigist, thank you for your unconditional love and everything that comes to my life with you. I will never forget your patience, sacrifices, and suffering that you endured in taking care of our children, especially when I stay late in office. I also want to acknowledge my daughter, Yeabsira, and my son, Elias. Yeabsira and Elias, I am so proud to be your father, you are sweet, positive, and cheerful kids. Finally, I would like to thank everybody who have contributed either directly or indirectly to this Thesis, as well as express my apology that I could not mention personally one by one.

Thank you!
Esubalewe Lakie Yedeg
Umeå, May 2016

I dedicate this thesis to
my mother, Wubit Aragaw, and
my beloved wife, Tigist Muluken.
I love you all dearly.

Contents

Chapter 1

Introduction

Mechanical devices play an important role in our daily life. How to "optimally" design them while satisfying the required system and design constraints is an important engineering concern. We assume that the optimality of the design can be measured by an objective function that quantifies, for example, construction cost, strength of the designed structure, or some other performance measure. If a particular design makes the objective function as high or low as possible, depending the objective, it is called an optimal design.

Numerical design optimization of mechanical devices seeks to acquire, using a combination of simulation and numerical optimization algorithms, the best performance of the device while satisfying some set of constraints. The subject is becoming more important due to material resource limitations, the development of computational algorithms, and the availability of high-performance computers. During the last three decades, the subject has developed rapidly with new theoretical insights, computational methods, and application areas. In general, numerical design optimization approaches can be classified into three main groups, namely *sizing optimization*, *shape optimization*, and *topology optimization*.

In sizing optimization, the conceptual geometry of the device is fixed during the optimization process, and the goal is to find the optimal values of some free parameters of the structure, such as thickness, length, or radius of individual components. In shape optimization problems, the shape of the boundaries is subject to optimization, but the conceptual layout is predetermined. The design variables are typically some kind of parameterization of the design boundaries. Topology optimization is the most general and flexible approach to numerical design optimization, where for every point in the design region, it is to be determined whether the point is occupied by a material or not. Thus, the shape as well as the connectedness of the individual parts of the structure are not known a priori. Topology optimization can be seen as a generalization of sizing and shape optimization.

The behaviour of mechanical devices can often be modeled by partial differential equations, such as the equations of elasticity, fluid mechanics, or acoustics. These models, ideally, represent the interaction of the device with its surroundings. Determin-

ing exact solutions of partial differential equations are possible only in some special cases. In general, finding approximate solutions of partial differential equations rely on numerical techniques. The finite element method is one of the major techniques for numerical solutions of partial differential equations.

Many mechanical systems can be modeled by ordinary differential equations. These systems change with respect to time or any other independent variable according to the equation. It is often possible to guide these systems from one state to another predefined state by applying some kind of external force or control. It may also be possible to carry out the same task in different ways. If there are more than one way of performing the task, then it may be possible to choose the "best" way. The best way can be quantified by using a measure of performance of the system; this measure is often called "cost function", "objective function", or "performance index". The external force applied to the system corresponding to the best performance is called the optimal control.

Optimal control also denotes the process of determining control and state trajectories for a system over a given period of time to minimize or maximize an objective function. Optimal control is related to the theory of calculus of variations. The theory of optimal control has been widely studied and is used in many areas since the beginning of the so-called "modern" control theory in the 1960s [1].

In general, control systems are classified into two broad categories: *closed loop* and *open loop* systems. In closed-loop systems, also called *feedback* control systems, the input is affected by the systems output directly or indirectly. It uses the input and some portion of the output to maintain a prescribed relationship between the output and the reference input. However, in open-loop control systems, sometimes called *off-line* or *non-feedback* control systems, the system output does not affect the control input in any form. In this case, the system is free from any change in response to the output of the process. Standard control theory mostly concerns closed-loop systems, and these are the ones used in most engineering control applications. In contrast, the open-loop systems are useful in more special situations. In this thesis, we consider the design of such open-loop systems.

In this thesis, we use the topology optimization and optimal control ideas in two different areas. First the topology optimization method is used to determine the internal layout of a reactive muffler to minimize the acoustic energy at the outlet. The method is also used to improve the far-field properties of an acoustic horn by distributing thin sound-hard material in the interior of the horn. We use the concept of acoustic transmission impedance to model the acoustic properties of thin material. A new finite element method for Helmholtz equation with embedded interface is formulated to numerically handle the transmission impedance. The Method of Moving Asymptotes [2] is used to solve the optimization problems. Finally, we apply the optimal control approach to determine the control of a ball pitching robot in order to throw a ball as far as possible. The open-loop control problem is solved numerically using Matlab's `fmincon`.

Chapter 2

Topology Optimization by Material Distribution

Topology optimization is a mathematical approach to optimize the material layout of a device within a given design space such that a certain performance criterion is maximized or minimized, depending the objective, for a given set of conditions. Starting from the publication of the pioneering paper by Bendsøe & Kikuchi [3], topology optimization methods for continuum structures have been expanded significantly and applied to many practical engineering problems. Topology optimization has been used starting from designing materials at micro-level, see for example the works of Sigmund [4], Zhou & Li [5], and Jensen et al. [6], to large-scale designs such as bridges and buildings, and for components within the automobile and aircraft industries, see for example the works of example Borrvall & Petersson [7], Guan et al. [8], Wang et al. [9], and Krog et al. [10].

The field of topology optimization is dominated by methods that apply the *material distribution* concept, that is, when the design variables somehow represent local material properties. Most numerical methods for topology optimization rely on finite element methods for performance evaluations. In this case, the design domain is discretized into a fine mesh of elements, and the purpose of the algorithm is to find the optimal material distribution by determining for each element in the design domain whether it should be filled with material (solid element) or not (element with air). In the next sections, a brief overview on topology optimization by the material distribution method is given.

2.1 Problem formulation

In general, a topology optimization problem consists of an objective function, a design domain, design constraints, and a state equation. Let Ω be the design domain and $\Omega_{\mathrm{m}} \subset \Omega$ the region in the design domain occupied by solid material. The distribution of material in Ω is usually modeled by a material indicator function α, defined as

$\alpha(x) = 1$, if $x \in \Omega_{\mathrm{m}}$ and $\alpha(x) = 0$ otherwise. Mathematically, a topology optimization problem in its general form is given by

$$\min_{\alpha \in U} J(\alpha, u) \tag{2.1a}$$

$$\text{s.t. } a(\alpha; u, v) = \ell(v) \quad \forall v \in \mathcal{V}, \tag{2.1b}$$

$$C(\alpha, u) \leq 0, \tag{2.1c}$$

where $U = \{\alpha : \alpha(x) \in \{0, 1\}, x \in \Omega\}$ is the set of admissible designs, J is an objective function to measure the performance, u denotes the state variable that solves the state equation, C is a constraint function, and $\mathcal{V}$ is an appropriate function space. The design and the state variables are related by the state equation, in this case given by the variational form (2.1b).

Remark: In acoustics related topology optimization problems, the material indicator function α is 1 in the region of air and 0 in the region that is occupied by sound-hard material.

The prototype problem of this kind is the classical problem of minimizing the compliance, $J = \ell(u)$ (equivalent to maximizing the stiffness), of a mechanical structure subject to state equation (2.1b), the governing equation of linear elasticity, and the volume constraint, $C(\alpha) = \int_\Omega \alpha(x)dx - V \leq 0$. Here, V is the upper bound of the volume occupied by solid material. To guarantee coercivity of the bilinear form, the material indicator function should not be zero. Therefore, the space of admissible designs $U = \{\alpha : \alpha(x) \in \{0, 1\}, x \in \Omega\}$ is usually replaced by $U = \{\alpha : \alpha(x) \in \{\varepsilon, 1\}, x \in \Omega\}$ for a small constant $\varepsilon > 0$, such that $\alpha(x) = \varepsilon$ for $x \in \Omega - \Omega_{\mathrm{m}}$.

In many cases, topology optimization problems of the form (2.1) are ill-posed. Typically, the ill-posedness is due to the existence of minimizing sequences that do not converge [11], which, after discretization, usually, manifests itself as mesh dependency in the numerical solution. A relaxation method can be used to address this problem. It also allows the use of gradient-based optimization algorithms. By letting α take values in the continuous range $[\varepsilon, 1]$, the binary optimization problem (2.1) becomes

$$\min_{\alpha \in \mathcal{U}} J(\alpha, u) \tag{2.2a}$$

$$\text{s.t. } a(\alpha; u, v) = \ell(v) \quad \forall v \in \mathcal{V}, \tag{2.2b}$$

$$C(\alpha, u) \leq 0, \tag{2.2c}$$

where $\mathcal{U} = \{\alpha : \varepsilon \leq \alpha(x) \leq 1, x \in \Omega\}$.

In the case of compliance minimization, there exist a unique solution of problem (2.2). The proof of the existence of a solution can be found in Section 5.2 of the book [12] by Bendsøe & Sigmund.

2.2 Discretization

Numerical methods are typically used to obtain an approximate solution of optimization problem (2.2). Following a finite element procedure, the domain Ω is partitioned into

N small subdomains called elements $E_k, k = 1, \ldots, N$, such that $\overline{\Omega} = \cup_{k=1}^{N} \overline{E}_k$. The material indicator function α is approximated by an element-wise constant function α_h. The state variable u is approximated by $u_h \in \mathcal{V}^h(\Omega)$, where $\mathcal{V}^h \subset \mathcal{V}$ is a space of continuous and element-wise polynomial functions. The discrete state variable u_h is the solution of the discrete state equation for a given feasible design α_h

$$a_h(\alpha_h; u_h, v_h) = \ell_h(v_h) \quad \forall v_h \in \mathcal{V}^h, \tag{2.3}$$

where v_h, a_h, and ℓ_h are the discretized version of v, a, and ℓ, respectively. Similarly, the objective and constraint functions are replaced by their corresponding discrete versions.

Then, the discrete version of the optimization problem (2.2) can be formulated as

$$\begin{aligned} \min_{\alpha_h \in \mathcal{U}_h} \; & J_h(\alpha_h, u_h) \\ \text{s.t. } & a_h(\alpha_h; u_h, v_h) = \ell_h(v_h) \quad \forall v_h \in \mathcal{V}^h, \\ & C_h(\alpha_h, u_h) \leq 0, \end{aligned} \tag{2.4}$$

where J_h and C_h are the discrete version of the objective and constraint functions, and the space of admissible designs, $\mathcal{U}_h$ is the set of element-wise constant functions. There are different optimization methods to solve the optimization problem (2.4), for instance, the optimality criteria method [13] and the Method of Moving Asymptotes (MMA) [2]. The MMA method is well suited mathematical algorithm for topology optimization problems [12]. We use the MMA to solve the topology optimization problem in Paper I.

2.3 Penalization

Unfortunately, the relaxed problem (2.2) is different from the original binary problem (2.1), and the material indicator function corresponding to the solution of the relaxed problem is usually not binary. This results in "gray" regions with α-values strictly between ε and 1 in the optimized designs. However, the goal of the original problem is to find a black and white structure, that is, a solution α such that $\alpha(x)$ is either ε or 1 for all points $x \in \Omega$. To obtain binary optimal designs, it is common to introduce some kind of penalization to force the intermediate values towards either ε or 1.

There are different penalization methods that can be used for this purpose. One of the methods, commonly used in acoustic related problems, deals with the intermediate values by adding a penalty function J_p to the objective function (2.2a), and optimizes the penalized problem

$$\min_{\alpha \in \mathcal{U}} J(\alpha, u) + \gamma J_p(\alpha) \tag{2.5a}$$

$$\text{s.t. } a(\alpha; u, v) = \ell(v) \quad \forall v \in \mathcal{V}, \tag{2.5b}$$

$$C(\alpha, u) \leq 0, \tag{2.5c}$$

where $\gamma > 0$ is a penalty parameter. Alternatively, the penalty function can be added as a constraint by including

$$J_p(\alpha) \leq \varepsilon_p,$$

in the problem (2.2), for a small positive number ε_p. One of the frequently used penalty functions [14, 15], is

$$J_p(\alpha) = \int_\Omega (1-\alpha)(\alpha - \varepsilon). \tag{2.6}$$

For topology optimization problems with *active* volume constraint, the so called Solid Isotropic Material with Penalization (SIMP) method is widely used. It was suggested by Bendsøe [16] and uses a non-linear interpolation function of the form

$$f_q(\alpha) = \alpha^q, \tag{2.7}$$

where $q > 1$ is a constant, together with the volume constraint

$$\int_\Omega \alpha(x)dx \leq V. \tag{2.8}$$

In this method, as the value of q increases the local stiffness of the intermediate values decreases while their volume remain unchanged.

Rietz [17] introduced a method, an alternating approach to the SIMP method, called RAMP (Rational Approximation of Material Properties) that uses

$$f_q(\alpha) = \frac{\alpha}{1+q(1-\alpha)}, \tag{2.9}$$

with $q > 0$. Both for SIMP and RAMP, the parameter q represents the amount of penalization, and the variational equation in problem (2.2) is replaced by

$$a(f_q(\alpha); u, v) = \ell(v) \quad \forall v \in \mathcal{V}, \tag{2.10}$$

with volume constraint (2.8).

2.4 Numerical instabilities and regularization

A well-organized survey of numerical instabilities in topology optimization for continuum elastic structures and their corresponding regularization methods is given by Sigmund & Petersson [11]. In this section, a brief overview of numerical instabilities and a possible treatment method is presented. In general, the common numerical problems arising in topology optimization can be categorized in to three groups: *mesh dependency*, formation of *checkerboard pattern*, and *local minima*.

Mesh dependency is the problem of finding qualitatively different solutions with more and more holes and finer structural elements with better performances when the problem is solved using the same algorithm but with finer and finer mesh sizes.

It is related to the non-existence of solution to the optimization problem, due to non-closedness of the set of feasible designs.

A checkerboard pattern is the occurrence of high oscillations of the design variable between air and material. The issue is usually associated with the choice of finite elements and can often be prevented by using higher-order finite elements for the state variable [18].

Most problems in topology optimization are not convex and many of them have multiple (local) minima [12]. Hence, performing the same numerical optimization algorithm but with a small change in the starting guess or algorithmic parameters can result different locally optimal solutions. Based on experience, a continuation approach is suggested to overcome this problem [11, 12]. This approach lets the penalization parameters increase or decrease gradually to guide the development of the solution towards reliably good designs.

In the literature, several methods are proposed to tackle the problems with checkerboard patterns and mesh-dependency in topology optimization [11, 12, 16]. Mesh-independent filtering methods are among the most commonly used methods due to their ease of implementation and their efficiency [19]. The use of filtering in topology optimization, based on ideas borrowed from image processing, was suggested by Sigmund [20]. Since then, filters have been used to regularize many topology optimization problems [15, 21, 22, 23]. Filtering methods for topology optimization can be grouped into *density* and *sensitivity* based methods.

Density filtering was introduced by Bruns & Tortorelli [21]. The main idea is to modify the element density such that it depends on the densities of elements in a predefined neighborhood. The problem is optimized with respect to an artificial density variable $\widehat{\alpha}$ and the physical density, the filtered one, is achieved by using a convolution of a filter kernel and the artificial density variable, given by

$$\alpha(x) = \int_{\mathbb{R}^d} \phi(x, y)\widehat{\alpha}(y)dy, \tag{2.11}$$

where d is the space dimenstion. A filter kernel ϕ that is commonly used for topology optimization is

$$\phi(x, y) = \sigma(x) \max\left(0, 1 - \frac{|x - y|}{\tau}\right), \tag{2.12}$$

where $\tau > 0$ is the filter radius and $\sigma(x)$ is a normalization factor such that

$$\int_{\mathbb{R}^d} \phi(x, y)dy = 1. \tag{2.13}$$

Bourdin [22] proved the existence of solutions as well as finite element convergence of the minimum compliance problem using this filter and the SIMP penalization method. In Paper I, we use density filtering with an anisotropic generalization of integration kernel (2.12) for an acoustic problem. The filtered and penalized version

of the topology optimization problem (2.2) is given by

$$\begin{aligned} &\min_{\widehat{\alpha}\in\mathcal{U}} J(\alpha,u)+\gamma J_p(\alpha) \\ &\text{s.t. } \alpha(\cdot)=\int_{\mathbb{R}^d}\phi(\cdot,y)\widehat{\alpha}(y)dy, \\ &\qquad a(\alpha;u,v)=\ell(v) \quad \forall v\in\mathcal{V}, \\ &\qquad C(\alpha,u)\leq 0. \end{aligned} \tag{2.14}$$

The other alternative, sensitivity filtering, is used to modify the design sensitivity of a particular element by making it dependent on a weighted average over its neighboring elements. In this method, the design updates are performed using the filtered sensitivity instead of the real sensitivity. The approach is simple to use but risky, especially for line-search based optimization algorithms [19]. Different variations of the two filtering methods are reviewed in Sigmund's article [19].

Chapter 3

Summary of Paper I - Interior layout topology optimization of a reactive muffler

3.1 Introduction

In Paper I, we consider the optimal design of a reactive muffler. A reactive muffler is a device commonly used to attenuate exhaust noise of internal combustion engines. It typically consists of a series of chambers of different dimensions connected together in order to cause an acoustic impedance mismatch, that is, to reflect a substantial part of the acoustic energy back to the source or back and forth among the chambers [24]. Any change in the arrangement or the dimensions of the muffler components affect the performance.

We use the material distribution approach to optimize the internal configuration of an expansion chamber in a cylindrically symmetric reactive muffler. The objective is to reduce the outgoing acoustic energy at the outlet as much as possible by distributing sound hard material inside the expansion chamber. We use Helmholtz equation to model the acoustic waves propagation in the muffler and a finite element method to numerically solve the equation. To solve the topology optimization problem, we use the Method of Moving Asymptotes, MMA [2].

3.2 Problem description

We consider a muffler consisting of an expansion chamber, an end inlet, and an end outlet as shown in Figure 3.1(a). There may be a perforated pipe connecting the inlet and the outlet. The computational domain $\Omega = \Omega^{\mathrm{l}} \cup \Omega^{\mathrm{u}}$ with $\Omega^{\mathrm{u}} = \Omega^{\mathrm{d}} \cup \Omega^{\mathrm{p}}$ is illustrated in Figure 3.1(b), which shows an arbitrary cross-section through the center of the cylindrically symmetric muffler 3.1(a). The non-overlapping regions Ω^{l} and Ω^{u} are separated by the interface Γ_{I}. The non-design region Ω^{l} is introduced to ensure unblocked gas flow from the inlet to the outlet. The optimization problem is to find an optimal distribution of sound-hard material in the gray-shaded design region Ω^{d} to

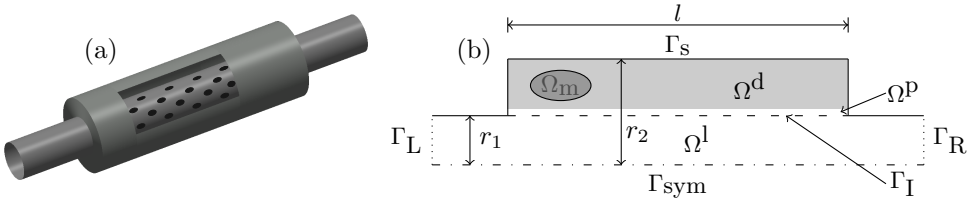

Figure 3.1: A cylindrical symmetric muffler and the computational domain.

improve the performance of the muffler. The region Ω^{m} in Figure 3.1(b) represents the region occupied by sound-hard material. The presence of material at each point in the design region is modeled by the material indicator function α, defined by $\alpha(x) = \varepsilon$ if $x \in \Omega^{\mathrm{m}}$ and $\alpha(x) = 1$ otherwise, where ε is a small positive number.

We ignore viscous losses, background flow, and hot gas effects in Ω. The inlet and outlet pipes are assumed to be narrow and long compared to the wavelength of interest, so that all non-planar modes of outgoing waves are geometrically evanescent and negligible at Γ_{L} and Γ_{R}. By assuming that the orifice diameter and the thickness of the perforated layer Γ_{I} are smaller than the wavelengths of interest, the sound propagation through the layer is modeled by an acoustic impedance.

Assume that the incoming wave at the inlet boundary, Γ_{L} is a plane wave of amplitude A. The Helmholtz equation, the boundary conditions, and the interface condition together results in the following variational problem.

$$
\begin{aligned}
&\text{Find } p^l \in H^1(\Omega^{\mathrm{l}}),\ p^u \in H^1(\Omega^{\mathrm{u}}) \text{ and } \lambda \in H^{-1/2}(\Gamma_{\mathrm{I}}) \text{ such that} \\
&\begin{cases}
\displaystyle\int_{\Omega^{\mathrm{l}}} r\nabla q^l \cdot \nabla p^l + \int_{\Omega^{\mathrm{u}}} \alpha r \nabla q^u \cdot \nabla p^u - \kappa^2 \int_{\Omega^{\mathrm{l}}} r q^l p^l \\
\quad -\kappa^2 \displaystyle\int_{\Omega^{\mathrm{u}}} \alpha r q^u p^u - \int_{\Gamma_{\mathrm{I}}} r[\![q]\!]\lambda + \mathrm{i}\kappa \int_{\Gamma_{\mathrm{L}}\cup\Gamma_{\mathrm{R}}} r q^l p^l = 2\mathrm{i}\kappa A \displaystyle\int_{\Gamma_{\mathrm{L}}} r q^l, \\
\qquad\qquad \displaystyle\int_{\Gamma_{\mathrm{I}}} r\mu[\![p]\!] - \frac{\mathrm{i}}{\kappa}\int_{\Gamma_{\mathrm{I}}} r\zeta\mu\lambda = 0,
\end{cases} \\
&\text{for all } q^l \in H^1(\Omega^{\mathrm{l}}),\ q^u \in H^1(\Omega^{\mathrm{u}}), \text{ and } \mu \in H^{-1/2}(\Gamma_{\mathrm{I}}),
\end{aligned}
\tag{3.1}
$$

where r is the radial coordinate, ζ is the acoustic impedance of the perforated layer, $\kappa = 2\pi f/c$ is the wavenumber for frequency f and speed of sound c, and $\mathrm{i}^2 = -1$. Functions $p = p^l$ and $p = p^u$ are the complex amplitude of the pressure field in Ω^{l} and Ω^{u}, respectively, and $[\![p]\!] = p^l - p^u$.

In order to allow the use of a gradient-based optimization algorithm, the binary constraint $\alpha \in \{\varepsilon, 1\}$ is relaxed into a box constraint $\alpha \in [\varepsilon, 1]$, and the optimization problem is formulated as a minimization of the transmission of acoustic energy to the muffler outlet for the target frequencies; that is,

$$
\min_{\widehat{\alpha}\in\mathcal{U}} \mathcal{J}(\widehat{\alpha}; \mathcal{W}, \gamma), \tag{3.2}
$$

where $\widehat{\alpha} \in \mathcal{U} = \{\beta \in L^\infty(\Omega) : 0 < \varepsilon \leq \beta \leq 1 \text{ a.e. in } \Omega^{\mathrm{d}}, \beta \equiv 1 \in \Omega - \Omega^{\mathrm{d}}\}$ is a new design variable, $\alpha = S(\widehat{\alpha})$ for filtering function $S : L^2(\mathbb{R}^2) \to L^2(\mathbb{R}^2)$, and $\mathcal{W}$ is the set of all frequencies for which we are interested in to optimize the muffler. The objective function is defined by

$$\mathcal{J}(\widehat{\alpha}; \mathcal{W}, \gamma) = J_p(S(\widehat{\alpha}); \gamma) + J_t(S(\widehat{\alpha}); \mathcal{W}). \tag{3.3}$$

Here, J_p is the penalty function, and the *primary* objective function J_t is defined by

$$J_t(\alpha; \mathcal{W}) = \sum_{f_j \in \mathcal{W}} J(p^l(\alpha, f_j)), \tag{3.4}$$

where for each $f_j \in \mathcal{W}$, $p^l(\alpha, f_j) \in H^1(\Omega^l)$ is part of the triplet p^l, p^u, and λ that solves state equation (3.1) for design α and wave number $\kappa = 2\pi f_j/c$. In expression (3.4), for a single frequency f_j, we define function J as the magnitude square of the mean pressure amplitude at the outlet boundary, that is

$$J(p^l(\alpha, f_j)) = \frac{1}{2}|\langle p^l \rangle_{\Gamma_{\mathrm{R}}}|^2, \tag{3.5}$$

where the mean acoustic pressure amplitude function over Γ_{R} is defined by

$$\langle p^l \rangle_{\Gamma_{\mathrm{R}}} = \frac{\int_{\Gamma_{\mathrm{R}}} r p^l}{\int_{\Gamma_{\mathrm{R}}} r}. \tag{3.6}$$

The finite element method is used to discretize problem (3.1). The material indicator function is assumed to be constant in each element. The Method of Moving Asymptotes solves optimization problem (3.3) by adding the penalty term to the objective function using a continuation approach for the penalty parameter γ. Post-processing techniques are used to sharpen the edges of the sound-hard material. The performance of the muffler designs are compared in terms of the transmission loss. The transmission loss of a muffler with the same cross-sectional area for the inlet and outlet is given by [25, 26]

$$TL = 10 \log_{10} \left(\frac{|p_i|^2}{|p_o|^2} \right), \tag{3.7}$$

where p_i and p_o are the amplitudes of the incoming and outgoing acoustic pressure, respectively.

3.3 Selected numerical results

Two types of reactive mufflers are considered for the optimization, with and without a perforated pipe connecting the inlet and the outlet. We denote them by *muffler with impedance layer* and *muffler without impedance layer*, respectively. The mufflers have the same general configuration; they have inlet and outlet pipes of radius $r_1 = 0.05$ m,

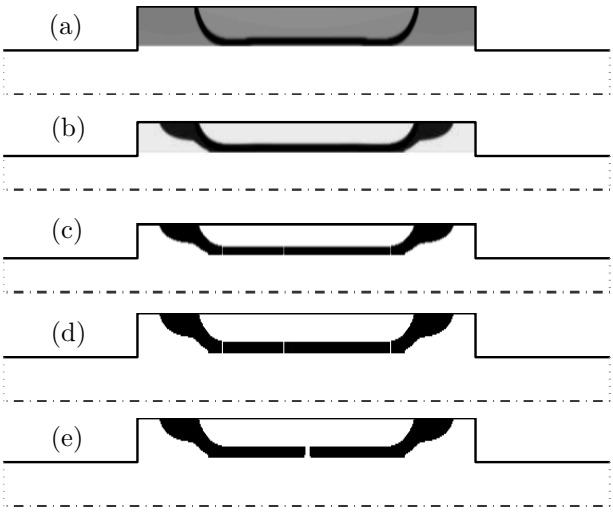

Figure 3.2: Final muffler designs from the continuation steps. (a) without penalty, (b) with penalty ($\gamma = 1/2$) and filter, (c) with penalty ($\gamma = 500$) and filter, (d) with penalty ($\gamma = 500$) and after filter is dropped, (e) after second level post-processing.

and the expansion chamber has radius $r_2 = 0.1$ m and length $l = 0.5$ m. The perforated pipe of the muffler with impedance layer is characterized by a porosity of $\sigma = 20\%$, thickness $t = 1.5$ mm, and orifice diameter $d = 3.1$ mm.

For all numerical experiments, we set $\epsilon = 10^{-8}$ as a lower bound for the design variable $\widehat{\alpha}_h$. We use 28,672 square elements with side length 1.5625 mm for the finite element discretization. The number of design variables is 9,280. We use an anisotropic filter of height 6.56 mm and width 3.28 mm. A plane wave of amplitude $A = 1$ is injected into the muffler at the inlet boundary. We verified the transmission loss spectra of the designs obtained from the optimization processes by using the Comsol Multiphysics software.

Figure 3.2 shows the designs from different steps of the continuation approach. The optimization is performed for a muffler without impedance layer at target frequency $f = 349$ Hz. Figures 3.2(a), 3.2(b), and 3.2(c) are the designs obtained from the optimization with $\gamma = 0$, $\gamma = 1/2$, and $\gamma = 500$, respectively. The figures show that as the parameter γ increases more and more, the designs become more black and white. Figure 3.2(c) looks black and white except at the edges of the sound-hard material. To obtain sharp edges, the filter is dropped and optimization is continued. Figure 3.2(d) shows the sharpened design. In this experiment, we add the second phase of post-processing, in which the three narrow openings in Figure 3.2(d) are replaced by a single opening of the same total width and the optimization without filter is restarted. Figure 3.2(e) shows the final design.

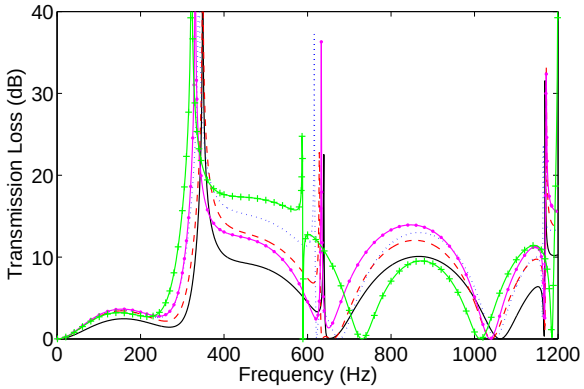

Figure 3.3: Transmission loss spectra corresponding to the designs in Figure 3.2. — TL of (a), – – TL of (b), ··· TL of (c), —●— TL of (d), —+— TL of (e).

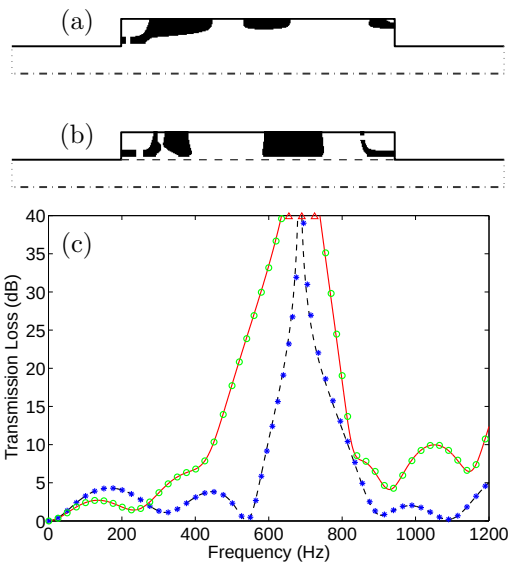

Figure 3.4: Final muffler designs for muffler (a) without and (b) with the perforated pipe, optimized for target frequency 697 Hz and corresponding transmission loss spectra (c): - - - for muffler (a) and —— for muffler (b). The asterisks and circles are the transmission losses computed by Comsol Multiphysics for the mufflers (a) and (b), respectively.

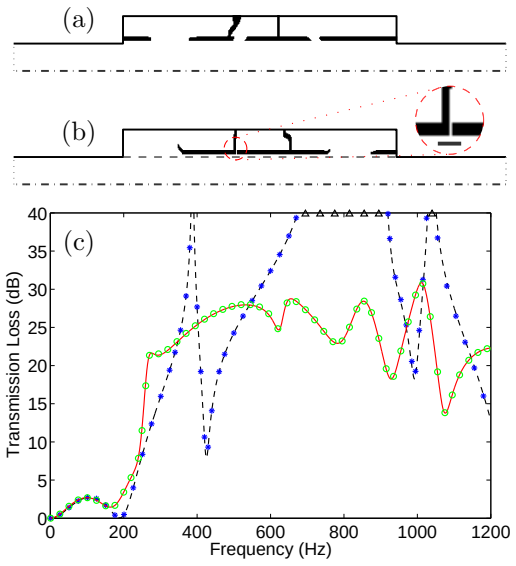

Figure 3.5: Final muffler designs for muffler (a) without and (b) with the perforated pipe, optimized for 20 target frequencies exponentially distributed in the range 250–1050 Hz and corresponding transmission loss spectra (c): - - - for muffler (a) and —— for muffler (b). The asterisks and circles are the transmission losses computed by Comsol Multiphysics for the mufflers (a) and (b), respectively. The close-up in figure (b) displays the narrow opening to the central resonating chamber.

We optimize the two types of mufflers for a single target frequency and for multi-target frequencies. The single frequency optimization is performed at 697 Hz. Figures 3.4(a) and 3.4(b) show the optimized design of the mufflers without and with impedance layer, respectively, and Figure 3.4(c) illustrates the transmission loss spectra of these two mufflers. The dashed line spectrum in Figure 3.4(c) shows that the design in Figure 3.4(a) performs remarkably good in the range 600–800 Hz. Similarly, the solid line spectrum shows that the design in Figure 3.4(b) has a good acoustic attenuation performance in the range 400–780 Hz.

To obtain a good performance in a wider range of frequencies, we optimize for 20 frequencies exponentially distributed in the range of 250–1050 Hz. The optimized layout of the mufflers without and with impedance layer are depicted in Figures 3.5(a) and 3.5(b), respectively. The corresponding transmission loss spectra are illustrated in Figure 3.5(c). The spectra show that the two mufflers perform remarkably good in the range 220–1200 Hz.

Chapter 4

Nitsche-Type Methods for Interface Problems

In his classical paper, Nitsche [27] proposed a new finite element method to solve a model Poisson problem with essential boundary condition. The method treats the boundary value problems without imposing the Dirichlet boundary condition in the finite element space, but instead modifies the variational problem to weakly enforce the boundary condition.

Another way to weakly enforce Dirichlet boundary conditions is through the use of Lagrangian multipliers [28]. Nitsche's method is closely related to the stabilized multiplier method of Barbosa & Hughes [29, 30], which circumvents the inf-sup condition that arises when Lagrangian multipliers are employed. The relation between the two methods is analysed by Stenberg [31]. Juntunen & Stenberg [32] extended Nitsche's method, designed for pure Dirichlet conditions, to a general class of mixed boundary conditions. Interior-penalty discontinuous Galerkin methods [33, 34] use the ideas of Nitsche to weakly enforce inter-element continuity. Stenberg [35] and Becker et al. [36] also use Nitsche's approach as a mortar method for domain decomposition with non-matching grids. Recently, Hansbo & Hansbo [37] proposed an unfitted finite element method to solve elliptic interface problem based on Nitsche's method.

As a background, we will discuss the Nitsche method for a standard elliptic interface problem, following the presentation in Hansbo & Hansbo [37] and Becker et al. [36]. Paper II extends this method to a complex-valued indefinite equation, the Helmholtz equation, and to a case with a much more complicated interface condition.

4.1 Problem formulation and preliminaries

Let Ω be an open bounded domain in $\mathbb{R}^n,\ n = 2, 3$ with a Lipschitz boundary $\partial\Omega$. As a model problem, we consider the following linear boundary value problem.

$$\begin{aligned} -\Delta u + u &= f \qquad \text{in } \Omega, \\ u &= 0 \qquad \text{on } \partial\Omega, \end{aligned} \tag{4.1}$$

where $f \in L^2(\Omega)$, the space of square integrable functions in Ω.

A variational form of problem (4.1) is formulated as follows.

$$\begin{aligned} &\text{Find } u \in H_0^1(\Omega) \text{ such that} \\ &a(u,v) = \int_\Omega fv \quad \forall v \in H_0^1(\Omega), \end{aligned} \tag{4.2}$$

where

$$a(u,v) = \int_\Omega (\nabla u \cdot \nabla v + uv), \tag{4.3a}$$

and $H_0^1(\Omega)$ denotes the set of functions in $L^2(\Omega)$ such that their first weak derivatives are also in $L^2(\Omega)$, and such that their trace on the $\partial\Omega$ vanish. Here, $L^2(\Omega)$ denote the space of square integrable functions on Ω.

Assume that Ω can be split into two disjoint, open, and connected subdomains Ω_1 and Ω_2 such that $\Omega = \Omega_1 \cup \Omega_2 \cup \Gamma_\mathrm{I}$, where $\Gamma_\mathrm{I} = \overline{\Omega}_1 \cap \overline{\Omega}_2$ is a smooth orientable interface boundary of codimension one with positive measure. We denote by $\boldsymbol{n}_1$ and $\boldsymbol{n}_2 = -\boldsymbol{n}_1$ the two unit normal fields on each side of the interface boundary. We fix an orientation of the interface by selecting one of these normals and denoting it by $\boldsymbol{n}$.

For a regular function u in $\Omega_1 \cup \Omega_2$, define u_i, $i = 1, 2$ as the limit of u when approaching the interface boundary from the interior of the side for which $\boldsymbol{n}_i$ is the outward-directed normal; that is, $u_i(\boldsymbol{x}) = \lim_{s\to 0^+} u(\boldsymbol{x} - s\boldsymbol{n}_i(\boldsymbol{x}))$ for $\boldsymbol{x} \in \Gamma_\mathrm{I}$, and we denote the jump of u over the interface by

$$[\![u]\!] = \boldsymbol{n} \cdot (\boldsymbol{n}_1 u_1 + \boldsymbol{n}_2 u_2), \tag{4.4}$$

and the average normal derivative over the interface is defined by

$$\left\{ \frac{\partial u}{\partial n} \right\} = \frac{1}{2} \left(\frac{\partial u_1}{\partial n} + \frac{\partial u_2}{\partial n} \right). \tag{4.5}$$

We then rewrite the model problem (4.1), due to the interface, as

$$-\Delta u + u = f \quad \text{in } \Omega_1 \cup \Omega_2, \tag{4.6a}$$
$$u = 0 \quad \text{on } \partial\Omega, \tag{4.6b}$$
$$[\![u]\!] = 0 \quad \text{on } \Gamma_\mathrm{I}, \tag{4.6c}$$
$$\left[\!\!\left[\frac{\partial u}{\partial n} \right]\!\!\right] = 0 \quad \text{on } \Gamma_\mathrm{I}. \tag{4.6d}$$

Here, note that $\partial\Omega = (\partial\Omega_1 \cup \partial\Omega_2) \setminus \Gamma_\mathrm{I}$. Problems (4.1) and (4.6) are equivalent.

Denote the space of square integrable functions on $\Omega_1 \cup \Omega_2$ by $L^2(\Omega_1 \cup \Omega_2)$. Let $\alpha = (\alpha_1, \ldots, \alpha_n) \in \mathbb{N}^n$ be a multi-index with $|\alpha| = \sum_{i=1}^n \alpha_i$. For a nonnegative integer m, $H^m(\Omega_1 \cup \Omega_2)$ denotes the set of functions $u \in L^2(\Omega_1 \cup \Omega_2)$ such that all weak

partial derivatives $\partial^\alpha u$ with $|\alpha| \leq m$ are also in $L^2(\Omega_1 \cup \Omega_2)$. Spaces $L^2(\Omega_1 \cup \Omega_2)$ and $H^m(\Omega_1 \cup \Omega_2)$ are equipped with norms

$$\begin{aligned} \|u\|^2_{L^2(\Omega_1 \cup \Omega_2)} &= \int\limits_{\Omega_1 \cup \Omega_2} |u|^2, \\ \|u\|^2_{H^m(\Omega_1 \cup \Omega_2)} &= \sum_{|\alpha| \leq m} \Big(\int\limits_{\Omega_1} |\partial^\alpha u|^2 + \int\limits_{\Omega_2} |\partial^\alpha u|^2 \Big), \end{aligned} \tag{4.7}$$

respectively. Note that the $H^m(\Omega_1 \cup \Omega_2)$ norms are "broken" norms that exclude the interface and that the space $H^m(\Omega_1 \cup \Omega_2)$ for $m \geq 1$ allows discontinuities over the interface.

For $i = 1, 2$, and a measurable subset $\Gamma \subset \partial\Omega_i$, we denote by $\gamma^{\Omega_i}_{\Gamma,m} : H^{m+1}(\Omega_i) \to H^{m+1/2}(\Gamma)$ the continuous, mth-order trace operator [38, Theorem 8.7], for which there is a constant c_1 such that

$$\|\gamma^{\Omega_i}_{\Gamma,m}\, u\|_{H^{m+1/2}(\Gamma)} \leq c_1 \|u\|_{H^{m+1}(\Omega_i)} \quad \forall u \in H^{m+1}(\Omega_i). \tag{4.8}$$

For $m = 0$ and 1, operator $\gamma^{\Omega_i}_{\Gamma,m}$ applied on $C^m\big(\overline{\Omega}_i\big)$ functions yield the restrictions of u and $\partial u/\partial n$ on Γ, respectively. In addition to inequality (4.8), the zeroth-order trace operator satisfies [39, Theorem 1.6.6]

$$\|\gamma^{\Omega_i}_{\Gamma,0}\, u\|^2_{L^2(\Gamma)} \leq c_2 \|u\|_{L^2(\Omega_i)} \|u\|_{H^1(\Omega_i)}, \quad i = 1, 2, \tag{4.9}$$

for some constant c_2. We denote the space of all measurable functions on Γ_{I} that are bounded almost everywhere by $L^\infty(\Gamma_{\mathrm{I}})$.

4.2 A Finite Element Method

We assume that $\Omega \subset \mathbb{R}^3$ has a polyhedral boundary and interface boundary Γ_{I} is polygonal. We introduce families of separate, non-degenerate tetrahedral triangulations $\big\{\mathcal{T}_1^h\big\}_{h>0}$ and $\big\{\mathcal{T}_2^h\big\}_{h>0}$ of Ω_1 and Ω_2, respectively, parameterized by $h = \max_{K \in \mathcal{T}_1^h \cup \mathcal{T}_2^h} h_K$, where h_K is the diameter of element $K \in \mathcal{T}_1^h \cup \mathcal{T}_2^h$. The condition of non degeneracy is that there exists a constant C such that for each $h > 0$ and $K \in \mathcal{T}_1^h \cup \mathcal{T}_1^h$, $h_K/\rho_K \leq C$, where ρ_K denotes the diameter of the largest ball contained in K. We note that if an element K satisfies condition $h_K/\rho_K \leq C$, then all faces F of K will satisfy the condition $h_F/\rho_F \leq C$, where h_F is the diameter of F and ρ_F is the diameter of the largest disc contained in F (see Section 3 in Paper II for further discussion).

We define the finite element space $V_h = V_1^h + V_2^h$, where V_i^h consists functions that are continuous on Ω_i, polynomials on each element in $\mathcal{T}_i^h$, and extended by zero into $\Omega \setminus \Omega_i$; that is,

$$V_i^h = \{v \in H^1(\Omega_1 \cup \Omega_2) \mid v\big|_K \in P_k(K)\ \forall K \in \mathcal{T}_i^h \text{ and } v \equiv 0 \text{ otherwise}\}, \tag{4.10}$$

where $P_k(K)$ denotes the polynomials of maximum degree $k \geq 1$ on element K.

The Nitsche-type method for the interface problem (4.6) is derived as follows. Assume that $u \in H^2(\Omega_1 \cup \Omega_2)$ satisfies interface problem (4.6). The continuity of normal derivatives, interface condition (4.6d), yields $\partial u_1/\partial n = \partial u_2/\partial n = \{\partial u/\partial n\}$. By multiplying equation (4.6a) by a test function $v \in H^1(\Omega_1 \cup \Omega_2)$ and applying integration by parts, using boundary condition (4.6b), we find that

$$\int_{\Omega_1 \cup \Omega_2} (\nabla u \cdot \nabla v + uv) - \int_{\Gamma_I} \left\{ \frac{\partial u}{\partial n} \right\} [\![v]\!] = \int_{\Omega_1 \cup \Omega_2} fv =: \ell(v). \tag{4.11}$$

Using interface condition (4.6c), equation (4.11) can be extended to

$$a_\lambda(u,v) := \int_{\Omega_1 \cup \Omega_2} (\nabla u \cdot \nabla v + uv) - \int_{\Gamma_I} \left\{ \frac{\partial u}{\partial n} \right\} [\![v]\!] - \int_{\Gamma_I} \left\{ \frac{\partial v}{\partial n} \right\} [\![u]\!] + \int_{\Gamma_I} \lambda [\![u]\!][\![v]\!] = \ell(v), \tag{4.12}$$

for any $\lambda \in L^\infty(\Gamma_I)$.

The Nitsche-type method for the interface problem, based on variational expression (4.12), is defined as follows.

$$\begin{aligned} &\text{Find } u_h \in V_h \text{ such that} \\ &\quad a_\lambda(u_h, v_h) = \ell(v_h) \quad \forall v_h \in V_h, \end{aligned} \tag{4.13}$$

where the parameter λ is a function of the mesh size h and a sufficiently large parameter $\gamma > 0$ (see Theorem 4.3.4 below).

4.3 Consistency and Coercivity

By the construction of the method, we have the following consistency lemma.

Lemma 4.3.1. A solution $u \in H^2(\Omega_1 \cup \Omega_2)$ of problem (4.2) satisfies

$$a_\lambda(u, v_h) = \ell(v_h) \quad \forall v_h \in V_h. \tag{4.14}$$

Lemma 4.3.1 implies Galerkin orthogonality; that is, if $u \in H^2(\Omega_1 \cup \Omega_2)$ solves problem (4.2) and u_h solves equation (5.4), then

$$a_\lambda(u - u_h, v_h) = 0 \quad \forall u_h \in V_h. \tag{4.15}$$

For the analysis of the method, we introduce the mesh dependent norm

$$|||\, u_h \,|||^2 = \int_{\Omega_1 \cup \Omega_2} (|\nabla u_h|^2 + |u_h|^2) + \int_{\Gamma_I} h \left| \left\{ \frac{\partial u_h}{\partial n} \right\} \right|^2 + \int_{\Gamma_I} \frac{1}{h} \left| [\![u_h]\!] \right|^2. \tag{4.16}$$

We need the following standard inverse inequality to prove coercivity of the bilinear form a_λ.

Lemma 4.3.2. For $v_h \in V_h$ there exist a constant C_I such that

$$\int_{\Gamma_I} h \left| \left\{ \frac{\partial v_h}{\partial n} \right\} \right|^2 \leq C_I \int_{\Omega_1 \cup \Omega_2} |\nabla v_h|^2. \tag{4.17}$$

Theorem 4.3.3 (Continuity). For any real and nonnegative $\lambda \in L^\infty(\Gamma_I)$, there is a constant C_c such that

$$a_\lambda(u, v) \leq C_c \, |||u||| \, |||v||| \quad \forall u, v \in V_h \cup H^2(\Omega). \tag{4.18}$$

Proof. Using Cauchy–Schwarz inequality, we bound the second and last term on the right side of expression (4.12) as follows

$$\int_{\Gamma_I} \left\{ \frac{\partial u}{\partial n} \right\} [\![v]\!] \leq \int_{\Gamma_I} \left| h \left\{ \frac{\partial u}{\partial n} \right\} \frac{1}{h} [\![v]\!] \right| \leq \Big(\int_{\Gamma_I} h \left| \left\{ \frac{\partial u}{\partial n} \right\} \right|^2 \int_{\Gamma_I} \frac{1}{h} \left| [\![v]\!] \right|^2 \Big)^{1/2} \tag{4.19}$$

and

$$\int_{\Gamma_I} \lambda [\![u]\!] [\![v]\!] \leq \Big(\int_{\Gamma_I} \lambda \left| [\![u]\!] \right|^2 \int_{\Gamma_I} \lambda \left| [\![v]\!] \right|^2 \Big)^{1/2}. \tag{4.20}$$

The bound for the third term on the right side of expression (4.12) follows similarly and as a result we have the continuity of a_λ. □

Next we show that, for a proper choice of parameter λ, the bilinear form a_λ is coercive.

Theorem 4.3.4 (Coercivity). Let γ be sufficiently large. Then, the bilinear form a_λ is coercive on V_h, that is,

$$a_\lambda(u_h, u_h) \geq C_\gamma \, |||u_h|||^2 \quad \forall u_h \in V_h, \tag{4.21}$$

for some $C_\gamma > 0$.

Proof. From the definition of a_λ, we have

$$a_\lambda(u_h, u_h) \geq \int_{\Omega_1 \cup \Omega_2} \Big(|\nabla u_h|^2 + |u_h|^2 \Big) - 2 \int_{\Gamma_I} \left| \left\{ \frac{\partial u_h}{\partial n} \right\} [\![u_h]\!] \right| + \int_{\Gamma_I} \lambda \left| [\![u_h]\!] \right|^2. \tag{4.22}$$

Consider the second term on the right side of expression (4.22). By inequalities (4.19) and $ab \leq a^2/2\varepsilon + \varepsilon b^2/2$, for any $\varepsilon > 0$, we get

$$2 \int_{\Gamma_I} \left| \left\{ \frac{\partial u_h}{\partial n} \right\} [\![u_h]\!] \right| \leq \int_{\Gamma_I} \frac{h}{\varepsilon} \left| \left\{ \frac{\partial u_h}{\partial n} \right\} \right|^2 + \int_{\Gamma_I} \frac{\varepsilon}{h} \left| [\![u_h]\!] \right|^2. \tag{4.23}$$

Substituting inequality (4.23) into expression (4.22) yields

$$a_\lambda(u_h,u_h) \geq \int\limits_{\Omega_1\cup\Omega_2} \Big(|\nabla u_h|^2 + |u_h|^2\Big) - \int\limits_{\Gamma_\mathrm{I}} \frac{h}{\varepsilon}\left|\left\{\frac{\partial u_h}{\partial n}\right\}\right|^2 + \int\limits_{\Gamma_\mathrm{I}} (\lambda - \frac{\varepsilon}{h})\Big|[\![u_h]\!]\Big|^2. \quad (4.24)$$

By adding and subtracting the second integral in expression (4.24) and using inequality (4.17), we get

$$\begin{aligned} a_\lambda(u_h,u_h) \geq \frac{1}{2}\int\limits_{\Omega_1\cup\Omega_2} \Big(|\nabla u_h|^2 + |u_h|^2\Big) + \int\limits_{\Gamma_\mathrm{I}} \frac{h}{\varepsilon}\left|\left\{\frac{\partial u_h}{\partial n}\right\}\right|^2 + \\ \Big(\frac{1}{2} - \frac{2C_I}{\varepsilon}\Big)\int\limits_{\Omega_1\cup\Omega_2} |\nabla v_h|^2 + \int\limits_{\Gamma_\mathrm{I}} (\lambda - \frac{\varepsilon}{h})\Big|[\![u_h]\!]\Big|^2. \end{aligned} \quad (4.25)$$

Choosing $\varepsilon = 4C_I$ and $\lambda = \gamma/h$ for $\gamma = 8C_I$ in inequality (4.26) yields

$$a_\lambda(u_h,u_h) \geq \frac{1}{2}\int\limits_{\Omega_1\cup\Omega_2} \Big(|\nabla u_h|^2 + |u_h|^2\Big) + \frac{2}{\gamma}\int\limits_{\Gamma_\mathrm{I}} h\left|\left\{\frac{\partial u_h}{\partial n}\right\}\right|^2 + \frac{\gamma}{2}\int\limits_{\Gamma_\mathrm{I}} \frac{1}{h}\Big|[\![u_h]\!]\Big|^2, \quad (4.26)$$

from which the coercivity follows with $C_\gamma = \min\big(2/\gamma, \gamma/2\big)$.

□

4.4 Convergence Analysis

Let π_i^h be the standard nodal interpolation operator [39, Def. 3.3.9] on the mesh $\mathcal{T}_i^h$ of Ω_i, and define the interpolation operator $\pi_h : W \to V_h$, where $W\big|_{\Omega_i} = H^m(\Omega_i) \cap C^0(\overline{\Omega}_i)$, by

$$\big(\pi_h q\big)\big|_{\Omega_i} = \pi_i^h\big(q\big|_{\Omega_i}\big) \qquad i = 1,2. \quad (4.27)$$

Then, the following local interpolation error estimate holds [39, Section 4.4], [40, Theorem 3.1.6]. For any $u \in H^m(K)$ and $0 \leq l \leq m$, we have

$$\|u - \pi_h u\|_{H^l(K)} = \|u - \pi_i^h u\|_{H^l(K)} \leq C h_K^{m-l} \|u\|_{H^m(K)} \;\forall K \in \mathcal{T}_i^h, i = 1,2. \quad (4.28)$$

From the local estimate the following lemma follows, stated without proof, which shows that the functions in V_h can approximate the functions $u \in H^{k+1}(\Omega_i)$ to the order of h^k in the triple norm $|||\cdot|||$ (see the work of Hansbo & Hansbo [41] for a similar proof).

Lemma 4.4.1 (Interpolation). Let π_h be as stated in expression (4.27). Then, for each $u \in H^{k+1}(\Omega_1 \cup \Omega_2)$, the following bound holds

$$|||u - \pi_h u||| \leq C_\pi h^s \|u\|_{H^{s+1}(\Omega_1\cup\Omega_2)}, \quad (4.29)$$

where C_π is independent of h and u, and $s \in [0,k]$ in which k is the maximal degree of the basis functions in V_h.

We now present the following a priori error estimates.

Theorem 4.4.2. Let $u \in H^{1+\sigma}(\Omega)$ for some $\sigma \geq 1$ be the solution of problem (4.2), and let $u_h \in V_h$ be a solution to the discrete problem (5.4). Then, there is a constant C such that

$$|||\, u - u_h \,||| \leq Ch^s \|u\|_{H^{s+1}(\Omega_1 \cup \Omega_2)}, \tag{4.30}$$

where $s = \min\{\sigma, k\}$.

Proof. For any $v_h \in V_h$, using coercivity (4.21), orthogonality (4.15), and continuity (4.18), we have

$$\begin{aligned} C_\gamma \, |||v_h - u_h|||^2 \leq & a_\lambda(v_h - u_h, v_h - u_h) \\ = & a_\lambda(v_h - u, v_h - u_h) \\ \leq & C_c \, |||v_h - u||| \, |||v_h - u_h|||, \end{aligned} \tag{4.31}$$

and hence

$$|||v_h - u_h||| \leq C_1 \, |||v_h - u|||, \tag{4.32}$$

where $C_1 = C_c/C_\gamma$. Now using triangle inequality, we obtain

$$|||u - u_h||| \leq |||u - v_h||| + |||v_h - u_h||| \leq C \, |||u - v_h|||, \tag{4.33}$$

where $C = 1 + C_1$. Finally, by choosing $v_h = \pi_h u$ and using Lemma 4.4.1, we get the desired result. □

Using standard duality techniques [39, §5.7], we can also show the a priori estimate

$$\| \, u - u_h \, \|_{L^2(\Omega_1 \cup \Omega_2)} \leq Ch^{s+1} \|u\|_{H^{s+1}(\Omega_1 \cup \Omega_2)}. \tag{4.34}$$

Chapter 5

Summary of Paper II - A Nitsche-type Method for Helmholtz Equation with an Embedded Acoustically Permeable Interface

5.1 Introduction

In the standard approach to material distribution based topology optimization, the material is distributed throughout the design region after the region is divided into finitely many small elements [12]. In this approach, a restriction method is typically needed to ensure mesh independent solutions. A restriction method, often realized through the use of filters, imposes a fixed minimal width of the distributed material. It is however possible to get significant effects on the propagation of acoustic waves, without adding extended volumes of materials, by an appropriate placement of thin structures with suitable material properties. Moreover, topology optimization without filtering applied to acoustic devices results in thin and scattered structures. It therefore appears natural to consider thin material distribution in acoustic devices design, instead of the "standard" material distribution approach to topology optimization [12]. The acoustic property of thin materials can be modeled by an acoustic transmission impedance of an embedded surface.

In Paper II, we present a Nitsche-type method for Helmholtz equation in which an interface, modeled by using a transmission impedance, is embedded in the computational domain. The method is conceptually similar to the approach of Hansbo & Hansbo [41] for the simulation of discontinuities in elasticity problems. Our method is designed to seamlessly handle a complex-valued impedance function that is allowed to vanish, for which the method reduces to a method analogous to the one in § 4.2 (symmetric interior-penalty method [33] to enforce interelement continuity).

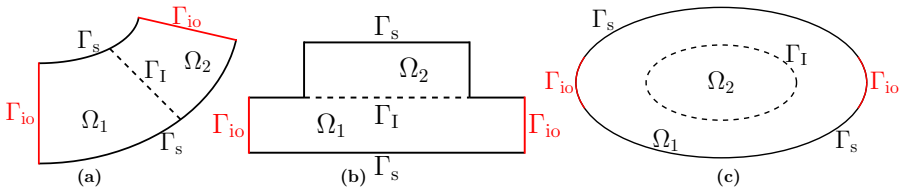

Figure 5.1: Computational domain cases.

5.2 Interface problems

Let Ω be an open bounded domain in $\mathbb{R}^n, n = 2, 3$ with a Lipschitz boundary $\partial\Omega$. Assume that Ω can be split into two disjoint, open, and connected subdomains Ω_1 and Ω_2 such that $\Omega = \Omega_1 \cup \Omega_2 \cup \Gamma_\mathrm{I}$, where $\Gamma_\mathrm{I} = \overline{\Omega}_1 \cap \overline{\Omega}_2$ is a smooth interface boundary of codimension one with positive measure. Assume that the boundary of $\Omega_1 \cup \Omega_2$ consists of the non-overlapping parts Γ_I, Γ_io, and Γ_s. See Figure 5.1 for illustrations.

The acoustic properties of the interface is modeled by a transmission impedance. Let the frequency-dependant function ζ defined on Γ_I denote the normalized acoustic impedance. We assume that $\operatorname{Re}\zeta \geq 0$, which means that acoustic energy may be absorbed but not created by the surface. The limits $|\zeta| \to 0$ and $|\zeta| \to \infty$ model a vanishing and a sound-hard surface, respectively. A special case is when $\operatorname{Im}\zeta < 0$. In this case, *surface waves* [42, § 3.2.4] can appear in a layer of depth $\delta = O(|\operatorname{Im}\zeta|/\kappa)$ around the surface for a (bulk) wavenumber κ. A local wave number associated with the surface waves increases with decreasing $|\operatorname{Im}\zeta|$.

We consider the following Helmholtz equation for acoustic pressure, in which the impedance condition with $\zeta \neq 0$, $\operatorname{Re}\zeta \geq 0$ is imposed on interface boundary Γ_I.

$$\Delta p + \kappa^2 p = 0 \qquad \text{in } \Omega_1 \cup \Omega_2, \tag{5.1a}$$

$$\mathrm{i}\kappa p + \frac{\partial p}{\partial n} = 2\mathrm{i}\kappa g \qquad \text{on } \Gamma_\mathrm{io}, \tag{5.1b}$$

$$\frac{\partial p}{\partial n} = 0 \qquad \text{on } \Gamma_\mathrm{s}, \tag{5.1c}$$

$$\frac{\mathrm{i}k}{\zeta}[\![p]\!] + \left\{\frac{\partial p}{\partial n}\right\} = 0 \qquad \text{on } \Gamma_\mathrm{I}, \tag{5.1d}$$

where $g \in L^2(\Gamma_\mathrm{io})$ is a given function, $[\![p]\!]$ and $\{\partial p/\partial n\}$ are the pressure jump and the average normal acoustic flux across the interface, defined in expressions (4.4) and (4.5), respectively.

A variational form of problem (5.1) is formulated as follows.

$$\begin{aligned} &\text{Find } p \in H^1(\Omega_1 \cup \Omega_2) \text{ such that} \\ &a(p, q) = 2\mathrm{i}\kappa \int_{\Gamma_\mathrm{io}} gq \quad \forall q \in H^1(\Omega_1 \cup \Omega_2), \end{aligned} \tag{5.2}$$

where

$$a(p,q) = \int_{\Omega_1\cup\Omega_2} \nabla p\cdot\nabla q - \kappa^2 \int_{\Omega_1\cup\Omega_2} pq + \mathrm{i}\kappa \int_{\Gamma_{\mathrm{io}}} pq + \mathrm{i}\kappa \int_{\Gamma_{\mathrm{I}}} \frac{1}{\zeta}[\![p]\!][\![q]\!]. \tag{5.3a}$$

In order for bilinear form a to be well defined on all of $H^1(\Omega_1\cup\Omega_2)\times H^1(\Omega_1\cup\Omega_2)$, we require that $\zeta\in L^\infty(\Gamma_{\mathrm{I}})$ such that $|\zeta|\geq\delta_\zeta$ almost everywhere for some constant $\delta_\zeta>0$. With this condition, the existence of a unique solution for problem (5.2) can be shown by using a Gårding inequality and compactness [38, § 17.4].

The proposed finite element method for the interface problem, which seamlessly handles both vanishing and non-vanishing interface conditions, is as follows.

$$\begin{aligned} &\text{Find } p_h\in V_h \text{ such that}\\ &\quad a_\lambda(p_h,q_h)=\ell(q_h)\quad \forall q_h\in V_h, \end{aligned} \tag{5.4}$$

where the space V_h of complex valued functions is as defined in Section 4.2 and

$$\begin{aligned} a_\lambda(p,q) =& \int_{\Omega_1\cup\Omega_2}\nabla p\cdot\nabla q - \kappa^2\int_{\Omega_1\cup\Omega_2} pq - \int_{\Gamma_{\mathrm{I}}}\left\{\frac{\partial p}{\partial n}\right\}\left([\![q]\!]+\frac{\zeta}{\mathrm{i}\kappa}\left\{\frac{\partial q}{\partial n}\right\}\right)+\int_{\Gamma_{\mathrm{I}}}\frac{\zeta}{\mathrm{i}\kappa}\left\{\frac{\partial p}{\partial n}\right\}\left\{\frac{\partial q}{\partial n}\right\}\\ &-\int_{\Gamma_{\mathrm{I}}}\left([\![p]\!]+\frac{\zeta}{\mathrm{i}\kappa}\left\{\frac{\partial p}{\partial n}\right\}\right)\left\{\frac{\partial q}{\partial n}\right\}+\int_{\Gamma_{\mathrm{I}}}\lambda\left([\![p]\!]+\frac{\zeta}{\mathrm{i}\kappa}\left\{\frac{\partial p}{\partial n}\right\}\right)\left([\![q]\!]+\frac{\zeta}{\mathrm{i}\kappa}\left\{\frac{\partial q}{\partial n}\right\}\right)+\mathrm{i}\kappa\int_{\Gamma_{\mathrm{io}}}pq \end{aligned} \tag{5.5}$$

with a complex-valued function

$$\lambda=\left(\frac{h}{\gamma}+\frac{\zeta}{\mathrm{i}\kappa}\right)^{-1} \tag{5.6}$$

for a sufficiently large $\gamma>0$ and for mesh parameter h. Function λ is nonzero and bounded under the requirement

$$h\,\mathrm{Im}\,\zeta\geq-\frac{\gamma}{4\kappa}|\zeta|^2 \qquad \text{almost everywhere on } \Gamma_{\mathrm{I}}. \tag{5.7}$$

By construction the method is consistent and symmetric. The stability of the method follows from the following theorem. Let Γ_{I}^- be the union of all subsets of Γ_{I} in which $\mathrm{Im}\,\zeta<0$ almost everywhere. Let $U=L^2(\Omega_1\cup\Omega_2)\times L^2(\Gamma_{\mathrm{I}}^-)$ and define the mapping $J:V\to U$ by $q\mapsto\big(\sqrt{\kappa}q,\,[\![q]\!]\big|_{\Gamma_{\mathrm{I}}^-}/\sqrt{\delta_\zeta}\big)$, which means that

$$\|Jq\|_U^2=\kappa\int_{\Omega_1\cup\Omega_2}|q|^2+\frac{1}{\delta_\zeta}\int_{\Gamma_{\mathrm{I}}^-}\big|[\![q]\!]\big|^2. \tag{5.8}$$

We note that J is injective and compact with an image that is dense in U.

Theorem 5.2.1. Let λ be as defined above, let condition (5.7) holds, and let γ be sufficiently large. Then, there is a constant C_c such that

$$|a_\lambda(p_h, q_h)| \leq C_c \,|||p_h||| \,|||q_h||| \quad \forall p_h, q_h \in V_h \cup H^2(\Omega_1 \cup \Omega_2). \tag{5.9}$$

Moreover, a_λ satisfies

$$|a_\lambda(p_h, p_h)| + 2\kappa \|Jp_h\|_U^2 \geq \frac{1}{4} |||\, p_h \,|||^2 \quad \forall p_h \in V_h, \tag{5.10}$$

where

$$|||\, p_h \,|||^2 = \int\limits_{\Omega_1 \cup \Omega_2} |\nabla p_h|^2 + \kappa^2 \int\limits_{\Omega_1 \cup \Omega_2} |p_h|^2 + \frac{1}{\gamma} \int\limits_{\Gamma_{\mathrm{I}}} h \left| \left\{ \frac{\partial p_h}{\partial n} \right\} \right|^2 + \int\limits_{\Gamma_{\mathrm{I}}} |\lambda| \left| [\![p_h]\!] \right|^2. \tag{5.11}$$

Assuming sufficient regularity of solutions to problem (5.2) and its dual, the following a priori error estimate holds.

Theorem 5.2.2. Assume that $\zeta \in L^\infty(\Gamma_{\mathrm{I}})$ satisfies $|\zeta| \geq \delta_\zeta > 0$ almost everywhere on Γ_{I}. Let p be the solution of problem (5.2), assumed to satisfy $p \in H^{1+\sigma}(\Omega_1 \cup \Omega_2)$ for some $\sigma \geq 1$, let p_h be a solution to the discrete problem (5.4), and let k denote the maximal polynomial order of the elements in V_h. Then, there exists a mesh size limit $h_1 > 0$ and a constant C such that for each $0 < h \leq h_1$,

$$|||\, p - p_h \,||| \leq C h^s |p|_{H^{s+1}(\Omega_1 \cup \Omega_2)}. \tag{5.12}$$

where $s = \min\{\sigma, k\}$.

5.3 Selected numerical results

Theorem 5.2.2 estimates the convergence rate of our method in the triple-norm. To study the L^2-convergence, we consider boundary value problem (5.1) in the domain $\Omega_1 \cup \Omega_2 = \{x \in \mathbb{R}^2 : 0 < |x_1| < 1, 0 < x_2 < 0.1\}$ with an interface boundary $\Gamma_{\mathrm{I}} = \{(0, x_2) \in \mathbb{R}^2 : 0 < x_2 < 0.1\}$. Since $\Omega_1 \cup \Omega_2$ is a narrow waveguide, the exact solution is given by

$$p(x_1, x_2) = \begin{cases} e^{-\mathrm{i}\kappa(x_1+1)} + \frac{\zeta}{2+\zeta} e^{\mathrm{i}\kappa(x_1-1)} & -1 < x_1 < 0,\ 0 < x_2 < 0.1, \\ \frac{2}{2+\zeta} e^{-\mathrm{i}\kappa(x_1+1)} & 0 < x_1 < 1,\ 0 < x_2 < 0.1. \end{cases} \tag{5.13}$$

Figure 5.2 shows the L^2-convergence of the new and standard finite element methods for $\zeta = 0.21 + 0.10\mathrm{i}$. Note that the curves for the standard and new methods are on top of each other. Numerical results also show that there is a similar convergence rate for a vanishing interface, $\zeta = 0$.

To observe the surface wave property, we solve boundary value problem (5.1) in $\Omega_1 \cup \Omega_2 \in \mathbb{R}^2$, which is an arbitrary cross-section of a simple cylindrical reactive muffler. Figure 5.3 shows the behaviour of the surface waves for varying bulk wave number κ and a fixed impedance $\zeta = -0.2\mathrm{i}$, whereas Figure 5.4 shows the behaviour for a fixed wave number κ and a varying impedance.

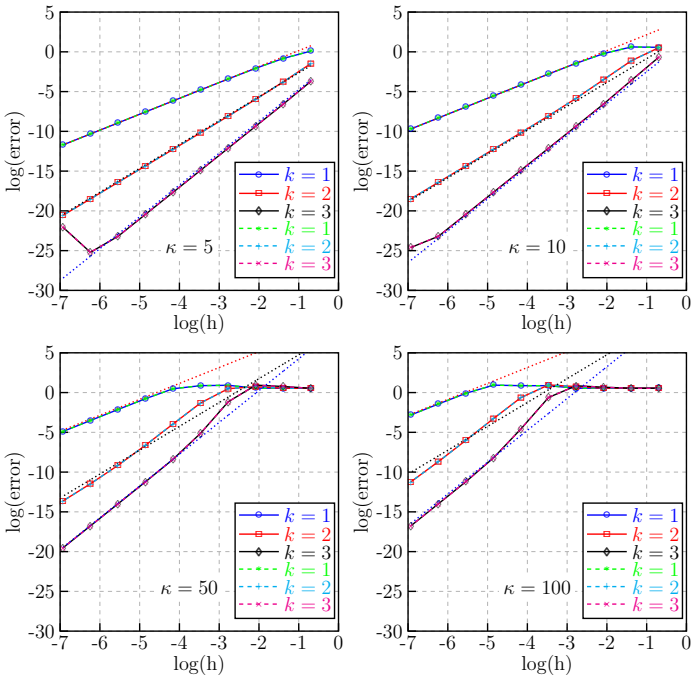

Figure 5.2: Convergence rates of the standard finite element and the proposed method for the interface problem with acoustic impedance $\zeta = 0.21 + 0.10\mathrm{i}$ for polynomial orders $k = 1$, $k = 2$, and $k = 3$, and wave numbers $\kappa = 5$, $\kappa = 10$, $\kappa = 50$, and $\kappa = 100$. The dotted lines are reference lines for second, third, and fourth order L^2-convergence.

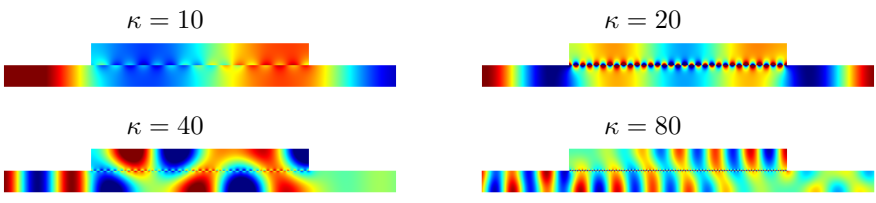

Figure 5.3: Surface waves corresponding to different wave numbers for $\zeta = -0.2\mathrm{i}$.

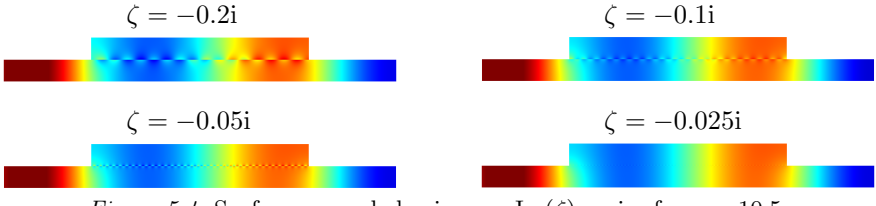

Figure 5.4: Surface waves behaviour as $\mathrm{Im}(\zeta)$ varies for $\kappa = 10.5$.

Chapter 6

Summary of Paper III and Paper IV - Layout optimization of thin sound-hard material to improve the far-field directivity properties of an acoustic horn

6.1 Introduction

In the material distribution to topology optimization [12], a design region is divided into a large number of small elements ("pixels" in 2D and "voxels" in 3D), and the optimization algorithm decides about the material composition of each element. The material distribution approach [12] is usually associated with techniques such as relaxation, penalization, and *design filters* to obtain mesh independent designs. This approach has the tendency to produce designs with extended volumes of material and to filter out thin structures. However, numerical experiences with optimization of devices for acoustic wave propagation have indicated a propensity for creation of thin (for example see Paper I) and scattered [43] structures, which are difficult to accomplish with the traditional topology optimization approach.

In Paper III, a material distribution approach to determine the layout of thin materials inside an acoustic horn is introduced. The acoustic properties of thin materials are modeled by an acoustic transmission impedance. We use the finite element method introduced in Chapter 5 to handle both vanishing and non-vanishing surface impedance simultanuously.

Paper IV outlines some technical details in connection to the problem treated in Paper III. In particular, it presents matrix representation for evaluations of the far-field pattern and the sensitivity analysis of the problem. We use the adjoint-based method [44, § 6] to efficiently compute the gradient of the objective function with respect to the design variables, and the accuracy of the gradient computation is verified against finite difference approximations.

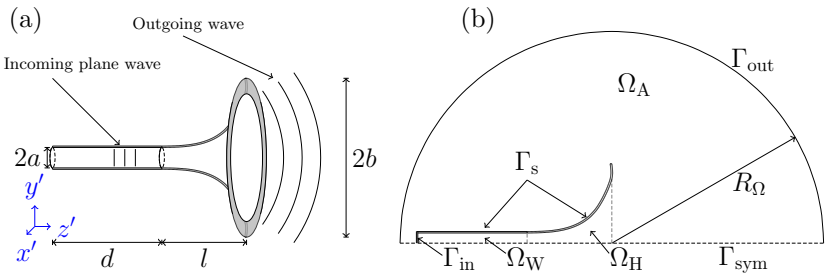

Figure 6.1: The horn to be optimized and the computational domain.

6.2 Problem description

We consider a cylindrically symmetric horn as shown in Figure 6.1a. The shape of the horn has already been determined by shape optimization aiming for a perfect transmission by minimizing the reflections of the horn back to its throat [45]. For the purpose of numerical computations, using the axial symmetry assumption, the exterior domain is truncated by an artificial far-field boundary Γ_{out}, which yields a bounded domain Ω, as depicted in Figure 6.1b. We assume that Ω is the union of three disjoint, open, and connected subdomains Ω_{W}, Ω_{H}, and Ω_{A}, that is, $\overline{\Omega} = \overline{\Omega}_{\text{W}} \cup \overline{\Omega}_{\text{H}} \cup \overline{\Omega}_{\text{A}}$. The boundaries of the computational domain are denoted by Γ_{out}; Γ_{in}, the left boundary of the truncated waveguide; Γ_{sym}, an axial symmetry line; and Γ_{s}, the boundary between sound-hard material and air.

Assume that the wave propagation is governed by the wave equation for the acoustic pressure P. By seeking a time harmonic solution, the time varying pressure field is separated as $P(x,t) = \operatorname{Re} p(x)\mathrm{e}^{\mathrm{i}\omega t}$, where Re is the real part, p is a complex amplitude function, ω is the angular frequency, $x = (r, z)$, and $\mathrm{i}^2 = -1$. The amplitude function p satisfies the Helmholtz equation

$$\frac{1}{r}\nabla \cdot (r\nabla p) + \kappa^2 p = 0 \text{ in } \Omega, \tag{6.1}$$

where $\kappa = \omega/c$ is the wavenumber, r is the radial coordinate, and $\nabla = (\partial/\partial r, \partial/\partial z)$.

Assume that the incoming wave at the inlet boundary Γ_{in} is a plane wave of amplitude A. The first order Engquist–Majda absorbing boundary condition is used to approximate the Sommerfeld radiation condition on Γ_{out} [46, 47]. Then, the complex amplitude function satisfies

$$\left(\mathrm{i}\kappa + \frac{1}{R_\Omega}\right) p + \frac{\partial p}{\partial n} = 0 \qquad \text{on } \Gamma_{\text{out}}, \tag{6.2a}$$

$$\mathrm{i}\kappa p + \frac{\partial p}{\partial n} = 2\mathrm{i}\kappa A \qquad \text{on } \Gamma_{\text{in}}, \tag{6.2b}$$

$$\frac{\partial p}{\partial n} = 0 \qquad \text{on } \Gamma_{\text{s}} \cup \Gamma_{\text{sym}}. \tag{6.2c}$$

To improve the performance of the given horn, we aim to distribute thin sheets of sound-hard material along a grid inside Ω_{H}. These squares partition the computational domain into several small subdomains and introduce numerous interface boundaries between the subdomains. We denote the union of all interface boundaries by Γ_{I} and define $\Omega_0 = \Omega \setminus \Gamma_{\mathrm{I}}$.

By assuming that the flux of the acoustic pressure is continuous over the interface, we have (see Section 2.1 of Paper II for the derivation)

$$\frac{\mathrm{i}k}{\zeta}[\![p]\!] + \left\{\frac{\partial p}{\partial n}\right\} = 0 \qquad \text{on } \Gamma_{\mathrm{I}}, \tag{6.3}$$

where ζ is the normalized transition impedance, and $[\![p]\!]$ and $\{\partial p/\partial n\}$ are the pressure jump and the average normal acoustic flux across the interface, respectively. Note that the limits $|\zeta| \to 0$ and $|\zeta| \to \infty$ model a vanishing and a sound-hard surface, respectively.

Helmholtz equation (6.1), together with boundary conditions (6.2) and interface condition (6.3), yields the following variational problem.

$$\begin{aligned} &\text{Find } p \in H^1(\Omega_0) \text{ such that} \\ &a(p,q) := a_0(p,q) + \mathrm{i}\kappa \int_{\Gamma_{\mathrm{I}}} \frac{r}{\zeta}[\![p]\!][\![q]\!] = 2\mathrm{i}\kappa A \int_{\Gamma_{\mathrm{in}}} rq \quad \forall q \in H^1(\Omega_0), \end{aligned} \tag{6.4}$$

where

$$a_0(p,q) = \int_{\Omega_0} r\nabla p \cdot \nabla q - \kappa^2 \int_{\Omega_0} rpq + \mathrm{i}\kappa \int_{\Gamma_{\mathrm{in}}\cup\Gamma_{\mathrm{out}}} rpq + \frac{1}{R_\Omega}\int_{\Gamma_{\mathrm{in}}} rpq. \tag{6.5}$$

We characterize the structure of Γ_{I} by a material indicator function $\alpha : \Gamma_{\mathrm{I}} \to \{0,1\}$ defined such that $\alpha(x) = 0$ if x is occupied by material and $\alpha(x) = 1$ if x is occupied by air. Then, we define the impedance function ζ such that $\zeta = 0$ when $\alpha = 1$, that is, for a vanishing interface, and such that ζ attains a large, purely imaginary value when $\alpha = 0$, that is, when approximating the impedance of a sound-hard material. To enable the use of gradient-based optimization algorithm, we relax the design variable, α to attain any value in the range $[0,1]$.

We introduce a collection of non-degenerate triangulations $\left\{\mathcal{T}_i^h\right\}_{h>0}$ of the subdomains Ω_i. Let V_i^h be the space of all complex-valued continuous functions that are bi-quadratic polynomials on each element in Ω_i and extended by zero into $\Omega \setminus \Omega_i$. We define the finite element space by $V_h = \sum_i V_i^h$. The solution of the acoustic problem $p \in H^1(\Omega_0)$ is approximated in the space V_h and denoted by p_h. The material indicator function α is approximated by an edge-wise constant function $\alpha_h : \Gamma_{\mathrm{I}} \to [0,1]$ and impedance function ζ is approximated by the edge-wise constant function $\zeta_h = \zeta(\alpha_h)$.

Based on a Nitsche-type formulation introduced in Chapter 5, the discrete variational problem which handles both vanishing and non-vanishing interface conditions is defined as follows.

$$\begin{aligned} &\text{Find } p_h \in V_h \text{ such that} \\ &\quad a_\lambda(p_h, q_h) = \ell(q_h) \quad \forall q_h \in V_h, \end{aligned} \tag{6.6}$$

where the discrete bilinear form a_λ is defined by

$$a_\lambda(p_h, q_h) = a_0(p_h, q_h) - \int_{\Gamma_I} (1 - \lambda \frac{\zeta_h}{\mathrm{i}\kappa}) \Big([\![q_h]\!] \Big\{ \frac{\partial p_h}{\partial n} \Big\} + [\![p_h]\!] \Big\{ \frac{\partial q_h}{\partial n} \Big\} \Big) - \int_{\Gamma_I} \frac{\zeta_h}{\mathrm{i}\kappa} (1 - \lambda \frac{\zeta_h}{\mathrm{i}\kappa}) \Big\{ \frac{\partial p_h}{\partial n} \Big\} \Big\{ \frac{\partial q_h}{\partial n} \Big\} + \int_{\Gamma_I} \lambda [\![p_h]\!] [\![q_h]\!], \tag{6.7}$$

in which the function $\lambda \in L^\infty(\Gamma_I)$ is as defined in expression (5.6).

6.3 Optimization problem

The objective of the optimization is to improve the far-field performance of the *reference horn* shown in Figure 6.1a while keeping the efficiency of the new design as high as possible. For single frequency f and a given design α_h, to minimize the reflection and the difference in magnitude of the far-field intensities at two given angles θ_1 and θ_2, we consider the objective functions

$$J_r^h(\alpha_h; f) = \frac{1}{2} |\langle p_h \rangle_{\Gamma_{\text{in}}} - A|^2, \tag{6.8a}$$

$$J_\infty^h(\alpha_h; f, \theta_1, \theta_2) = \frac{1}{2} \Big| \log_{10} \left(\frac{|p_{h,\infty}(\theta_1)|^2}{|p_{h,\infty}(\theta_2)|^2} \right) \Big|, \tag{6.8b}$$

where $\langle p_h \rangle_{\Gamma_{\text{in}}}$ is the mean acoustic pressure over Γ_{in}, as defined in expression (3.6), and p_h is the solution of problem (6.6) for a $\kappa = 2\pi f/c$ and $\zeta_h = \mathrm{i}\zeta_{\max}(1 - \alpha_h)^3$; $\zeta_{\max}$ is chosen such that $\zeta_h = \mathrm{i}\zeta_{\max}$ approximates the impedance of sound-hard material. Here the far-field pattern at an angle θ is defined by

$$p_{h,\infty}(\theta) = \frac{1}{4\pi} \int_{\Gamma_{\text{out}}} e^{\mathrm{i}\kappa \widehat{x} \cdot x} \left(\frac{1}{R_\Omega} + \mathrm{i}\kappa + \mathrm{i}\kappa \widehat{x} \cdot n \right) p_h, \tag{6.9}$$

where $\widehat{x}(\theta)$ is a point on the unit sphere at an angle θ with respect to the symmetry axis. Then, the objective function used for the optimization is given by

$$J^h(\alpha_h; \mathcal{F}, \Theta) = \frac{1}{n_f} \sum_{i=1}^{n_f} J_r^h(\alpha_h; f_i) + \frac{1}{n_f(n_\theta - 1)} \sum_{i=1}^{n_f} \sum_{j=1}^{n_\theta - 1} J_\infty^h(\alpha_h, f_i, \theta_j, \theta_{j+1}), \tag{6.10}$$

where $\mathcal{F} = \{f_1, f_2, \ldots, f_{n_f}\}$ and $\Theta = \{\theta_1, \theta_2, \ldots, \theta_{n_\theta}\}$ are the set of considered frequencies and angles, respectively. The set of feasible designs is defined by

$$\mathcal{U}_h = \Big\{ \alpha_h \in L^\infty(\Gamma_I) : 0 \le \alpha_h \le 1 \text{ a.e. in } \Gamma_I \Big\}. \tag{6.11}$$

6.4 Sensitivity Analysis

Let a_i denote the value of the piecewise constant functions α_h on boundary mesh element E_i in Γ_{I}, and define the vector representation of α_h by $\mathbf{a} = (a_1, \ldots, a_{N_\Gamma})^T$, where N_Γ is the number of interface boundary elements. For a single frequency f and angles θ_1 and θ_2, consider the objective function

$$J_h(\mathbf{a}; f, \theta_1, \theta_2) = \frac{1}{2} \log_{10} \left(\frac{|p_{h,\infty}(\theta_1)|^2}{|p_{h,\infty}(\theta_2)|^2} \right). \tag{6.12}$$

The derivative of $J_h$with respect to a_i, using the chain rule and the adjoint-based computation, is (see Paper IV for the full derivation)

$$\frac{\partial J(\mathbf{a}; f, \theta_1, \theta_2)}{\partial a_i} = \frac{G(\theta_1) - G(\theta_2)}{\ln(10)}, \tag{6.13}$$

where

$$G(\theta) = \frac{1}{|p_{h,\infty}(\theta)|^2} \left(\operatorname{Re} p_{h,\infty}(\theta) \operatorname{Re} \frac{\partial p_{h,\infty}(\theta)}{\partial a_i} + \operatorname{Im} p_{h,\infty}(\theta) \operatorname{Im} \frac{\partial p_{h,\infty}(\theta)}{\partial a_i} \right). \tag{6.14}$$

Here, Im is the imaginary part and

$$\begin{aligned} \frac{\partial p_{h,\infty}}{\partial a_i} = \int_{E_i} \frac{dc_1}{da_i} r \left([\![z_h]\!] \left\{ \frac{\partial p_h}{\partial n} \right\} + [\![p_h]\!] \left\{ \frac{\partial z_h}{\partial n} \right\} \right) + \\ \int_{E_i} \frac{dc_2}{da_i} r \left\{ \frac{\partial z_h}{\partial n} \right\} \left\{ \frac{\partial p_h}{\partial n} \right\} - \int_{E_i} \frac{d\lambda}{da_i} r [\![z_h]\!] [\![p_h]\!], \end{aligned} \tag{6.15}$$

with

$$\begin{aligned} \frac{d\lambda}{da_i} &= -\frac{1}{\mathrm{i}\kappa} \lambda_i^2 \frac{d\zeta_{h,i}}{da_i}, \\ \frac{dc_1}{da_i} &= -\frac{1}{\mathrm{i}\kappa} \left(\lambda_i - \frac{1}{\mathrm{i}\kappa} \lambda_i^2 \zeta_{h,i} \right) \frac{d\zeta_{h,i}}{da_i}, \\ \frac{dc_2}{da_i} &= \frac{1}{\mathrm{i}\kappa} \left(1 - \frac{\zeta_{h,i}}{\mathrm{i}\kappa} \left(2\lambda_i - \frac{1}{\mathrm{i}\kappa} \lambda_i^2 \zeta_{h,i} \right) \right) \frac{d\zeta_{h,i}}{da_i}, \end{aligned} \tag{6.16}$$

where $\lambda_i = \lambda|_{E_i}$, $\zeta_{h,i} = \zeta_h(a_i)$, and z_h is the solution to the following adjoint problem.

$$\begin{aligned} &\text{Find } z_h \in V_h \text{ such that} \\ &\quad a_\lambda(\alpha_h; v_h, z_h) = v_{h,\infty}(\theta) \quad \forall v_h \in V_h, \end{aligned} \tag{6.17}$$

where

$$v_{h,\infty}(\theta) = \frac{1}{4\pi} \int_{\Gamma^{3d}_{\text{out}}} e^{\mathrm{i}\kappa \widehat{x} \cdot x} \left(\frac{1}{R_\Omega} + \mathrm{i}\kappa + \mathrm{i}\kappa \widehat{x} \cdot n \right) v_h. \tag{6.18}$$

Note that the derivative $d\zeta_{h,i}/da_i$ in expression (6.16) depends on the parametrization of $\zeta_{h,i}$. The accuracy of the gradient computation in expression (6.13) is verified against finite difference approximations in Paper IV.

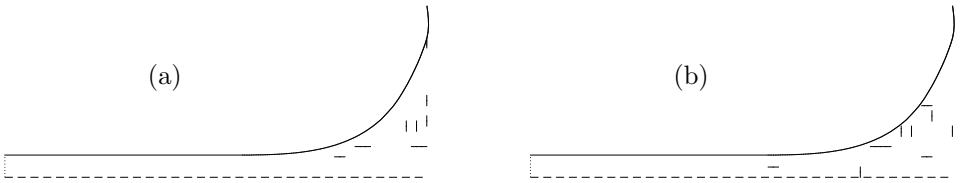

Figure 6.2: Final horn designs: (a) optimized for three target frequencies $6400 \times 2^{(m-2)/12}$ Hz, for $m = 0, 1, 2$ and (b) optimized for nine target frequencies $6400 \times 2^{(m-2)/12}$ Hz, $0, 1, \ldots, 8$.

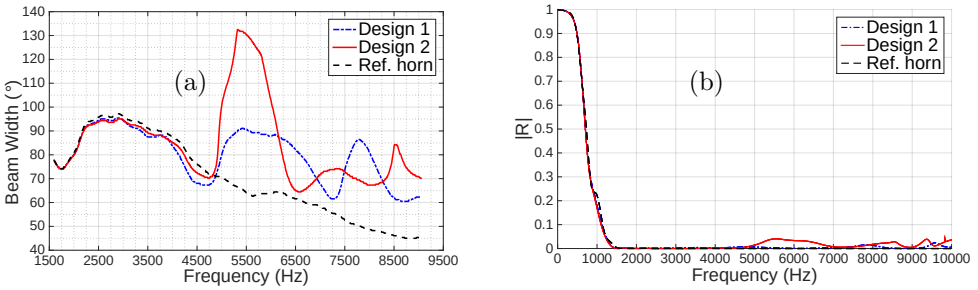

Figure 6.3: The beam width and reflection spectrum as functions of frequency of the optimzed horns in Figure 6.2 and the reference horn. Design 1 and Design 2 refer to the designs in Figures 6.2a and 6.2b, respectively, and Ref. Horn is the reference horn.

6.5 Selected numerical results

We consider the reference horn depicted in Figure 6.1a with length $l = 161.5$ mm, throat radius $a = 19.3$ mm, and mouth radius $b = 150$ mm. The waveguide has a radius of $a = 19.3$ mm and a length of $d = 206.5$ mm. The horn region Ω_{H}, illustrated in Figure 6.1b, is divided into 68 subdomains by putting 67 squares with side length 8.9722 mm. The boundaries between the subdomains form the interface Γ_{I} consisting of 146 components. The reference horn has virtually perfect transmission properties within the considered frequency range. The reflection spectrum of the reference horn is plotted in Figure 6.3b (dashed line). However, the far-field properties of the reference horn are not ideal, in particular for higher frequencies. The beam width of the reference horn is plotted in Figure 6.3b (dashed line). We optimize the horn for an even far-field directivity at angles 0°, 5°, 10°, 15°, 20°, and 25° with respect to the symmetry axis.

Figures 6.2a and 6.2b show the final designs of the horn optimized for three target frequencies $6400 \times 2^{(m-2)/12}$ Hz, for $m = 0, 1, 2$ and nine target frequencies $6400 \times 2^{(m-2)/12}$ Hz, $0, 1, \ldots, 8$, respectively. Figure 6.3a shows the beam width of the two optimized designes depicted in Figure. 6.2 using the dash-dotted and solid lines, respectively. The beam width for the two designs are uniformly above 60° in frequency band 1600 to 9050 Hz. The reflection spectra of the designs in Figures 6.2a and 6.2b, and the reference horn are shown in Figure 6.3b.

Chapter 7

Summary of Paper V - State constrained optimal control of a ball pitching robot

7.1 Introduction

In Paper V, we study an optimal control problem of a ball pitching robot that is designed to capture important dynamics of the human upper limb (including the shoulder, arm, and forearm) during an overarm throw. The robot has two links that are connected at the *elbow* joint by a linear torsional spring. The links represent the arm and forearm, and the spring represents the stiffness of the muscles around the elbow joint in human upper limb [48, 49]. The two-link robot is connected to a motor shaft at the *shoulder* joint by a non-linear torsional spring. At the end of the forearm, the robot is equipped with a gripping mechanism that allows the robot to grasp and release the ball at any required time.

The main objective is to determine the optimal motor torque and the release time that enable the robot to pitch the ball as far as possible. We include constraints on the motor torque and power as well as the angular velocity of the motor shaft into the problem formulation. For computational efficiency, we replace the time-global constraints on maximum allowed power and maximum angular velocity of the motor shaft by approximations based on integral quantities.

7.2 Problem formulation

The initial configuration of the two-link robot with a gripping mechanism holding a ball is illustrated in Figure 7.1. We denote the two links by the *arm* and *forearm*, respectively. Let q_2 measure the angle change between the arm and the forearm at the elbow joint. The angles q_1 and q_m, measured with respect to the horizontal axis, describe the configuration of the arm and the motor shaft, respectively. The only driving force of the system comes from the motor shaft. Figure 7.2 shows a trajectory

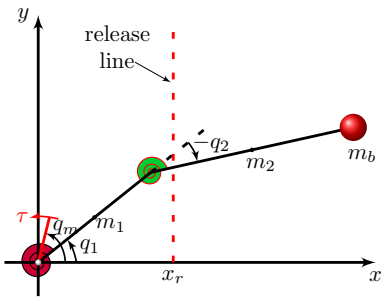

Figure 7.1: Initial configuration of the pitching robot and the release line.

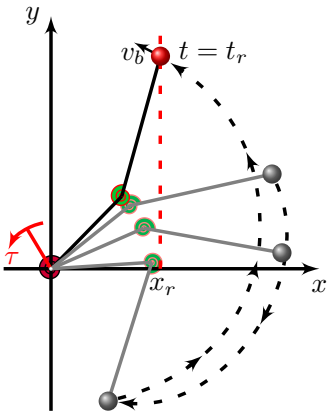

Figure 7.2: Configuration of the pitching robot at the release time and the ball trajectory during the pitching motion.

of the ball during a pitching motion. The ball gets released with velocity v_b when it crosses the release line $(x, y) = (x_r, s), s \in \mathbb{R}^+$.

Let $q = [q_m, q_1, q_2]^T$ be a vector of generalized coordinates of the robotic manipulator and let $\theta(t) = [q(t), \dot{q}(t)]^T \in \mathbb{R}^6$ be the state vector. Let $\tau(t) \in \mathbb{R}$ be a variable that measures the torque of the motor*. The equations of motion of the system, derived based on the Euler–Lagrange formulation in Appendix A of Paper V, in state space representation becomes

$$\dot{\theta} = f(\theta, \tau), \tag{7.1}$$

where

$$f(\theta, \tau) = \begin{bmatrix} \theta_4 \\ \theta_5 \\ \theta_6 \\ I_m^{-1}(\tau - \tau_s(\theta)) \\ M(\theta)^{-1}\left(K(\theta) - G(\theta) - C(\theta)\begin{bmatrix}\theta_4 \\ \theta_5\end{bmatrix}\right) \end{bmatrix}, \tag{7.2}$$

and where I_m is the motor inertia, $\tau_s(\theta)$ the torque due to the non-linear spring at the shoulder joint, $M(\theta)$ the inertia matrix, $C(\theta)$ the matrix of centrifugal and Coriolis forces, and where the vectors $G(\theta)$ and $K(\theta)$ represent gravitational and spring forces, respectively.

As illustrated in Figure 7.2, at time $t = t_r$ the ball is released with velocity v_b. It then follows a ballistic trajectory until it hits the ground at a point $(J, 0)$, where

$$J(\theta, x_r) = x_r + \frac{\dot{x}_b(t_r)}{g}\left(\dot{y}_b(t_r) + \sqrt{\dot{y}_b(t_r)^2 + 2g y_b(t_r)}\right). \tag{7.3}$$

Here x_r is the position of the vertical release line $(x, y) = (x_r, s)$, $s \in \mathbb{R}^+$, at which the gripping mechanism of the robot releases the ball, and g is the gravitational constant.

*In the published paper, Figures 1 and 2, τ is erroneously denoted by τ_m.

The vertical position of the ball at the release time is

$$y_b(t_r) = l_1 \sin(q_1(t_r)) + l_2 \sin(q_1(t_r) + q_2(t_r)),$$

where l_1 and l_2 are the lengths of the arm and forearm, respectively. Similarly, the velocity of the ball $v_b = (\dot{x}_b, \dot{y}_b)$ at time $t = r_r$ is given by

$$\begin{aligned} \dot{x}_b(t_r) &= -l_1 \sin(q_1(t_r))\dot{q}_1(t_r) - l_2 \sin(q_1(t_r) + q_2(t_r))(\dot{q}_1(t_r) + \dot{q}_2(t_r)), \\ \dot{y}_b(t_r) &= l_1 \cos(q_1(t_r))\dot{q}_1(t_r) + l_2 \cos(q_1(t_r) + q_2(t_r))(\dot{q}_1(t_r) + \dot{q}_2(t_r)). \end{aligned} \tag{7.4}$$

Note that the robot's shoulder is held fixed at the origin of the coordinate system and that the ball is thrown in the negative x direction. Hence, minimizing J implies maximizing the distance between the origin and the point $(J, 0)$.

We minimize J over the torque change in time. By inclusion of the constraints on the motor torque and torque change in the set of admissible controls, we obtain

$$\mathcal{A} = \left\{ \eta \in L^\infty \mid \sup_t |\eta(t)| \leq C_\tau, \ \sup_t \left| \tau_0 + \int_0^t \eta(s)\, \mathrm{d}s \right| \leq \bar{\tau} \right\}, \tag{7.5}$$

where $\bar{\tau}$ is the maximum allowed torque of the motor, C_τ is the bound on the torque change in time, and η is the control function defined by

$$\begin{aligned} \dot{\tau} &= \eta, \\ \tau(0) &= \tau_0. \end{aligned} \tag{7.6}$$

For computational efficiency, we replace the time-global constraints on maximum allowed power and maximum angular velocity of the motor shaft by approximations based on integral quantities (see Paper V for further discussion). Since it is possible to determine the release line position if the release time is known and vice versa, we optimize with respect to the release line position instead of the time.

Putting the system dynamics, the objective function, and the constraints together, we obtain the optimal control problem

$$\begin{aligned} \min_{\eta \in \mathcal{A},\, x_r} \quad & J(x_r, \theta(t_r)) \\ \text{s.t.} \quad & \dot{\tau} = \eta, \ \ \tau(0) = \tau_0, \\ & \dot{\theta} = f(\theta, \tau), \ \ \theta(0) = \theta^{(0)}, \\ & \left(\frac{1}{t_r} \int_0^{t_r} |\theta_4|^p \, \mathrm{d}t \right)^{1/p} \leq \left(\frac{1}{p+1} \right)^{1/p} Q_{\max}, \\ & \left(\frac{1}{t_r} \int_0^{t_r} |\tau\theta_4|^p \, \mathrm{d}t \right)^{1/p} \leq \left(\frac{1}{p+1} \right)^{1/p} P_{\max}, \end{aligned} \tag{7.7}$$

where $Q_{\max}$ and $P_{\max}$ are the maximum allowed angular velocity of the motor shaft and input power of the motor, respectively, and $\theta^{(0)}$ is the initial state of the system.

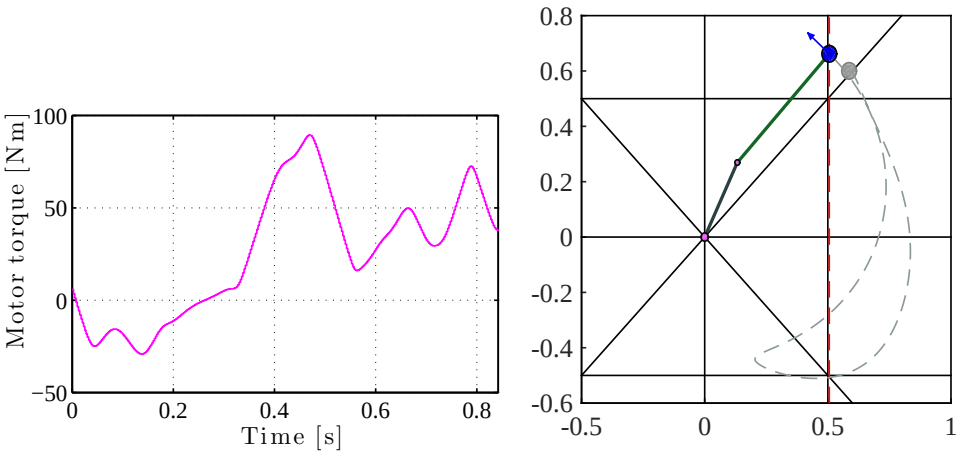

Figure 7.3: Left: the time evaluation of the optimal torque. Right: the ball trajectory during the pitching motion, starting from the initial position up to the time when the ball is released.

To numerically solve optimal control problem (7.7), we use a uniform discretization of the time interval $[0, T]$, where T is a sufficiently large time such that $0 < t_r \leq T$. Then, we use the so-called *Heun's method* to numerically solve the state equation. The discrete version of optimal control problem (7.7) is solved numerically by an interior point method with BFGS Hessian approximation as implemented in Matlab's `fmincon`. The gradients of the objective function and the constraint functions are computed using the adjoint method.

7.3 Selected numerical results

The non-linear spring at the shoulder joint produces a torque that is approximated by the function

$$\tau_s = 7761.7(q_m - q_1)^3 + 2.9755(q_m - q_1)^2 + 77.8080(q_m - q_1) - 0.0334. \tag{7.8}$$

The coefficients are obtained from a least-squares fit with measured data, for the ball pitching robot we study, in the range $|q_m - q_1| \leq 0.25$ rad. In this range, the relative error between the measured data and the cubic model is less than 2.5×10^{-3}. The initial conditions

$$q_0 = [0.978, 0.908, -0.172] \text{ rad}^\dagger, \;\; \dot{q}_0 = 0 \text{ rad/s}, \text{ and } \tau_0 = 8.213 \text{ Nm} \tag{7.9}$$

are determined in such away that the system is stationary at time $t_0 = 0$ for a given $q_1(0) = \pi - 2.234$ rad. The lengths of the arm and the forearm are $l_1 = 0.3$ m and

[†] In the published paper, the order of the elements in q_0 is erroneous.

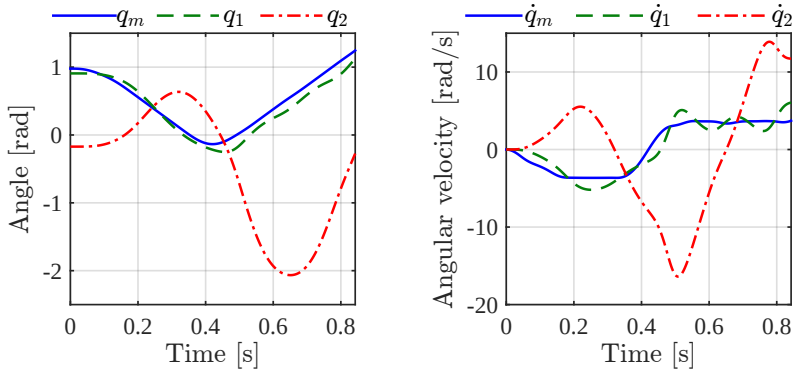

Figure 7.4: Time evolution of the generalized coordinates q_m, q_1, and q_2 (left), the corresponding angular velocities $\dot{q}_m, \dot{q}_1$, and $\dot{q}_2$ (right) computed using the optimal input torque from Figure 7.3.

$l_2 = 0.542$ m, respectively. The maximum allowed motor torque, power, and angular velocity of the motor shaft are $\bar{\tau} = 180$ Nm, $P_{\max} = 270$ Nm/s, and $Q_{\max} = 3.787$ rad/s, respectively. For a complete set of parameters for this experiment refer to Paper V. We set $T = 2$ s, $\Delta t = 0.0025$ s, $C_\tau = 1000$ Nm/s, and $p = 100$ for the numerical experiments.

Figure 7.3 shows the time evaluation of the resulting optimal input torque profile (left diagram) and the ball trajectory during the pitching motion (right diagram). The torque profile shows that the optimal torque attains its maximum value 89.54 Nm after 0.473 s. The optimal release line given by $(x, y) = (x_r, s)$, where $x_r = 0.506$ m and $s \in \mathbb{R}^+$, and the pitching motion takes $t_r = 0.843$ s to cross the release line. The ball is thrown at an upward angle of 40.82 degrees with velocity of 11.36 m/s. After the ball is released, it follows a ballistic trajectory in the negative direction and finally hits the ground 13.25 m away from the origin (the robot's shoulder position).

Figure 7.4 illustrates the time evolution, from the initial time to the final time, of the generalized coordinates q_1, q_2, and q_m (left diagram), and the angular velocities $\dot{q}_1, \dot{q}_2$, and $\dot{q}_m$ (right diagram). Recall that q_2 measures the angle change between the arm and the forearm, while q_1 and q_m measure the angle of the arm and the motor shaft with respect to the horizontal line. The left diagram illustrates, in particular, that $|q_m - q_1| \leq 0.25$ rad throughout the motion.

From the right diagram of Figure 7.4, we can see that the angular velocity $\dot{q}_m$ of the motor shaft (solid line) essentially has four phases. Starting from a stationary position, in the first phase it decelerates from a stationary position until it reaches an angular velocity of about -3.7 rad/s. The motor shaft moves at an almost constant angular velocity in the second phase, and accelerates rapidly in the third phase. Finally, the motor shaft moves at a relatively constant angular velocity of about 3.7 rad/s. In the second and last phase the angular speed $\dot{q}_m$ of the motor shaft reached to the

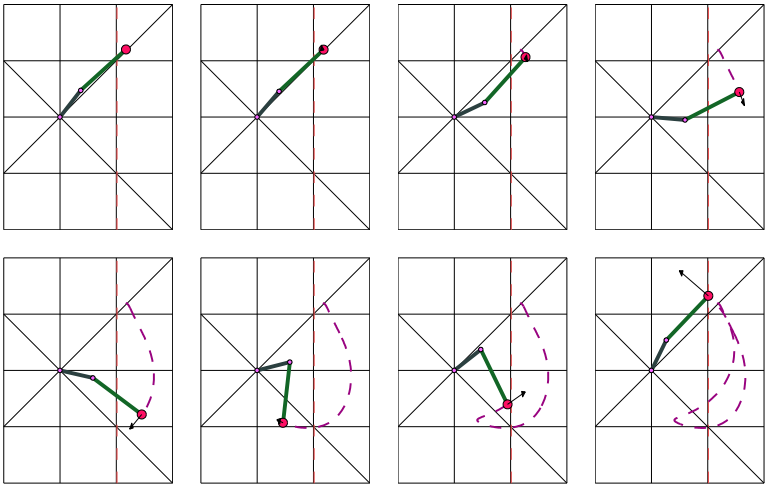

Figure 7.5: Snapshots of the ball pitching robot during the throwing motion obtained by using the optimal input torque presented in Figure 7.3. The snapshots are taken at times (top row from left to right) $t = 0$, $t_r/7$, $2t_r/7$, and $3t_r/7$ and (bottom row from left to right) $t = 4t_r/7$, $5t_r/7$, $6t_r/7$, and t_r, where $t_r = 0.843$ s is the duration of the throwing motion.

maximum bound. During the last 0.35 s, the angular velocity, $\dot{q}_1 + \dot{q}_2$ of the forearm measured with respect to the horizontal line is strictly increasing.

Figure 7.5 shows snapshots, taken at equal time interval, of the robot and illustrates the trajectory of the ball during the throwing motion. The snapshots suggest that about three quarters of the total pitching time is spent on swinging the ball backward against the throwing direction to get longer interval of acceleration. In the last quarter of the pitching time, the arm and forearm swings forward to the direction of the throw and the ball accelerates rapidly and reaches its maximum velocity at the release line.

Bibliography

[1] D. Kirk, Optimal Control Theory: An Introduction, Dover Books on Electrical Engineering Series, Dover Publications, 2004.

[2] K. Svanberg, The method of moving asymptotes–a new method for structural optimization, International Journal for Numerical Methods in Engineering 24 (1987), pp. 359–373.

[3] M. Bendsøe, N. Kikuchi, Generating optimal topologies in structural design using a homogenization method, Computer Methods in Applied Mechanics and Engineering 71 (1988), pp. 197–224.

[4] O. Sigmund, Tailoring materials with prescribed elastic properties, Mechanics of Materials 20 (1995), pp. 351–368.

[5] S. Zhou, Q. Li, Design of graded two-phase microstructures for tailored elasticity gradients, Journal of Materials Science 43 (2008), pp. 5157–5167.

[6] K. Jensen, P. Szabo, F. Okkels, Topology optimization of viscoelastic rectifiers, Applied Physics Letters 100 (2012), pp. 234102-1–234102-3.

[7] T. Borrvall, J. Petersson, Large-scale topology optimization in 3d using parallel computing, Computer Methods in Applied Mechanics and Engineering 190 (2001), pp. 6201–6229.

[8] H. Guan, Y. Chen, Y. Loo, Y. Xie, G. Steven, Bridge topology optimization with stress, displacement and frequency constraints, Computers and Structures 81 (2003), pp. 131–145.

[9] L. Wang, P. Basu, J. Leiva, Automobile body reinforcement by finite element optimization, Finite Elements in Analysis and Design 40 (2004), pp. 879–893.

[10] L. Krog, A. Tucker, M. Kemp, R. Boyd, Topology optimization of aircraft wing box ribs, in: 10th AIAA/ISSMO Multidisciplinary Analysis and Optimization Conference (2004), pp. 1–16.

[11] O. Sigmund, J. Petersson, Numerical instabilities in topology optimization: A survey on procedures dealing with checkerboards, mesh-dependencies and local minima, Structural optimization 16 (1998), pp. 68–75.

[12] M. Bendsøe, O. Sigmund, Topology optimization. Theory, methods, and applications, Springer, 2003.

[13] O. Sigmund, A 99 line topology optimization code written in matlab, Structural and Multidisciplinary Optimization 21 (2001), pp. 120–127.

[14] C. Jog, R. Haber, Stability of finite element models for distributed-parameter optimization and topology design, Computer Methods in Applied Mechanics and Engineering 130 (1996), pp. 203–226.

[15] T. Borrvall, J. Petersson, Topology optimization using regularized intermediate density control, Computer Methods in Applied Mechanics and Engineering 190 (2001), pp. 4911–4928.

[16] M. Bendsøe, Optimal shape design as a material distribution problem, Structural and Multidisciplinary Optimization 1 (1989), pp. 193–202.

[17] A. Rietz, Sufficiency of a finite exponent in SIMP (power law) methods, Structural and Multidisciplinary Optimization 21 (2001), pp. 159–163.

[18] A. D´iaz, O. Sigmund, Checkerboard patterns in layout optimization, Structural optimization 10 (1995), pp. 40–45.

[19] O. Sigmund, Morphology-based black and white filters for topology optimization, Structural and Multidisciplinary Optimization 33 (2007), pp. 401–424.

[20] O. Sigmund, Design of Material Structures Using Topology Optimization, PhD thesis, Technical University of Denmark, 1994.

[21] T. Bruns, D. Tortorelli, Topology optimization of non-linear elastic structures and compliant mechanisms, Computer Methods in Applied Mechanics and Engineering 190 (2001), pp. 3443–3459.

[22] B. Bourdin, Filters in topology optimization, International Journal for Numerical Methods in Engineering 50 (2001), pp. 2143–2158.

[23] M. Wang, S. Wang, Bilateral filtering for structural topology optimization, International Journal for Numerical Methods in Engineering 63 (2005), pp. 1911–1938.

[24] L. Munjal, Acoustics of ducts and mufflers with application to exhaust and ventilation system design, Wiley-Interscience publication, Wiley, 1987.

[25] T. Wu, G. Wan, Muffler performance studies using a direct mixed–body boundary element method and a three-point method for evaluating transmission loss, Journal of Vibration and Acoustics 118 (1996), pp. 479–484.

[26] D. Davis, G. Stokes, D. Moore, G. Stevens, Theoretical and experimental investigation of mufflers with comments on engine-exhaust muffler design, NACA technical report 1192 (1954), pp. 829–875.

[27] J. Nitsche, Über ein Variationsprinzip zur Lösung von Dirichlet-Problemen bei Verwendung von Teilräumen, die keinen Randbedingungen unterworfen sind, Abhandlungen aus dem Mathematischen Seminar der Universität Hamburg 36 (1971), pp. 9–15.

[28] I. Babuška, The finite element method with Lagrange multiplayer, Numerische Mathematik 20 (1973), pp. 179–192.

[29] H. Barbosa, T. Hughes, The finite element method with Lagrange multipliers on the boundary: circumventing the Babuška-Brezzi condition, Computer Methods in Applied Mechanics and Engineering 85 (1991), pp. 109–128.

[30] H. Barbosa, T. Hughes, Boundary Lagrange multipliers in finite element methods: Error analysis in natural norms, Numerische Mathematik 62 (1992), pp. 1–15.

[31] R. Stenberg, On some techniques for approximating boundary conditions in the finite element method, Journal of Computational and Applied Mathematics 63 (1995), pp. 139–148.

[32] M. Juntunen, R. Stenberg, Nitsche's method for general boundary conditions, Mathematics of Computation 78 (2009), pp. 1353–1374.

[33] D. Arnold, An interior penalty finite element method with discontinuous elements, SIAM Journal on Numerical Analysis 19 (1982), pp. 742–760.

[34] D. Arnold, F. Brezzi, B. Cockburn, L. Marini, Unified analysis of discontinuous Galerkin methods for elliptic problems, SIAM Journal on Numerical Analysis 39 (2002), pp. 1749–1779.

[35] R. Stenberg, Mortaring by a method of J. A. Nitsche, Computational Mechanics, New Trends and Applications (1998), pp. 1–6.

[36] R. Becker, P. Hansbo, R. Stenberg, A finite element method for domain decomposition with non-matching grids, ESAIM Mathematical Modelling and Numerical Analysis 37 (2003), pp. 209–225.

[37] A. Hansbo, P. Hansbo, An unfitted finite element method, based on Nitsche's method, for elliptic interface problems, Computer Methods in Applied Mechanics and Engineering 191 (2002), pp. 5537–5552.

[38] J. Wloka, Partial Differential Equations, Cambridge University Press, 1987.

[39] S. Brenner, R. Scott, The Mathematical Theory of Finite Element Methods, Texts in Applied Mathematics, Springer, 2008.

[40] P. Ciarlet, The Finite Element Method for Elliptic Problems, Society for Industrial and Applied Mathematics, Philadelphia, PA, USA, 2002.

[41] A. Hansbo, P. Hansbo, A finite element method for the simulation of strong and weak discontinuities in solid mechanics, Computer Methods in Applied Mechanics and Engineering 193 (2004), pp. 3523–3540.

[42] S. Rienstra, A. Hirschberg, An introduction to acoustics, Revised and updated version of reports IWDE 92-06 and IWDE 01-03, Eindhoven University of Technology, 2015.

[43] E. Wadbro, R. Udawalpola, M. Berggren, Shape and topology optimization of an acoustic horn–lens combination, Journal of Computational and Applied Mathematics 234 (2010), pp. 1781–1787.

[44] P. Christensen, A. Klarbring, An Introduction to Structural Optimization, volume 153 of *Solid Mechanics and Its Applications*, Springer, 2008.

[45] D. Noreland, R. Udawalpola, P. Seoane, E. Wadbro, M. Berggren, An efficient loudspeaker horn designed by numerical optimization: An experimental study, Technical Report UMINF 10.1, Department of Computing Science, Umeå University, 2010.

[46] B. Engquist, A. Majda, Absorbing boundary conditions for the numerical simulation of waves, Mathematics of Computation 31 (1977), pp. 629–651.

[47] F. Ihlenburg, Finite Element Analysis of Acoustic Scattering, Springer, New York, 1998.

[48] S. Katsumata, S. Ichinose, T. Shoji, S. Nakaura, M. Sampei, Throwing motion control based on output zeroing utilizing 2-link underactuated arm, in: The 2009 American Control Conference (2009), pp. 3057–3064.

[49] U. Mettin, A. Shiriaev, L. Freidovich, M. Sampei, Optimal ball pitching with an underactuated model of a human arm, in: IEEE International Conference on Robotics and Automation (2010), pp. 5009–5014.